The contribution of AGN and star-forming galaxies to the Mid-Infrared as revealed by their Spectral Energy Distributions

C. Gruppioni[(1)a], F. Pozzi[(2)], M. Polletta[(3,4)], G. Zamorani[(1)], F. La Franca[(5)], N. Sacchi[(5)], A. Comastri[(1)], L. Pozzetti[(1)], C. Vignali[(2)], C. Lonsdale[(6)], M. Rowan-Robinson[(7)], J. Surace[(6)], D. Shupe[(6)], F. Fang[(6)], I. Matute[(8)], S. Berta[(9)]

ABSTRACT

We present the broad-band Spectral Energy Distributions (SEDs) of the largest available highly (72%) complete spectroscopic sample of mid-infrared (MIR) selected galaxies and AGN at intermediate redshift. The sample contains 203 extragalactic sources from the 15-μm survey in the ELAIS-SWIRE field S1, all with measured spectroscopic redshift. Most of these sources have full multi-wavelength coverage from the far-UV (*GALEX*) to the far-infrared (*Spitzer*) and lie in the redshift range $0.1 < z < 1.3$. Due to its size, this sample allows us for the first time to characterise the spectral properties of the sources responsible for the strong evolution observed in the MIR. Based on SED-fitting technique we have classified the MIR sources, identifying AGN signatures in about 50% of them. This fraction is significantly higher than that derived from optical spectroscopy ($\sim$29%) and is due in particular to the identification of AGN activity in objects spectroscopically classified as galaxies. This might be partially due to the fact that the spectroscopic classification can be somewhat unreliable because

[(1)]INAF: Osservatorio Astronomico di Bologna, via Ranzani 1, I–40127 Bologna, Italy

[a] e-mail: carlotta.gruppioni@oabo.inaf.it

[(2)]Dipartimento di Astronomia, Università di Bologna, via Ranzani 1, I–40127 Bologna, Italy

[(3)]Institut d'Astrophysique de Paris, 98bis blvd Arago, Paris 75014, France

[(4)]INAF: IASF Milano, via Bassini 15, I–20133 Milano, Italy

[(5)]Dipartimento di Fisica, Università degli Studi "Roma Tre", via della Vasca Navale 84, I–00146 Roma

[(6)]Infrared Processing and Analysis Center, California Institute of Technology 100-22, Pasadena, CA 91125, USA

[(7)]Astrophysics Group, Blackett Laboratory, Imperial College of Science Technology and Medicine, Prince Consort Road, London SW7 2BZ, UK

[(8)]INAF: Osservatorio Astrofisico di Arcetri, Largo E. Fermi 5, I–50125 Firenze, Italy

[(9)]Dipartimento di Astronomia, Universitá di Padova, vicolo Osservatorio 2, I–35122 Padova, Italy

of host galaxy dilution in the optical. It is likely that in most of our objects, the AGN is either obscured or of low-luminosity, and thus it does not dominate the energetic output at any wavelength, except in the MIR, showing up just in the range where the host galaxy SED has a minimum. The fraction of AGN strongly depends on the flux density, with that derived through the SED-fitting being about 20% at $S_{15\mu m} \sim 0.5 - 1$ mJy and gradually increasing up to 100% at $S_{15\mu m} > 10$ mJy, while that obtained from optical spectroscopy never being >30%, even at the higher flux densities. The results of this work will be very useful for updating all the models aimed at interpreting the deep infrared survey data and, in particular, for constraining the nature and the role of dust-obscured systems in the intermediate/high-redshift Universe.

Subject headings: infrared: galaxies – galaxies: evolution – galaxies: Seyfert – galaxies: starburst – cosmology: observations.

1. Introduction

Understanding the overall Spectral Energy Distribution (SED) of sources responsible for the observed Cosmic Infrared Background (CIRB) is a crucial tool for unveiling the nature and evolution of galaxies and AGN in the infrared (IR) and for obtaining a complete picture of the history of star-formation and obscured AGN activity in the Universe. The mid- and far-infrared (MIR and FIR) regions of the electromagnetic spectrum efficiently probe the population of actively star-forming galaxies and dust-obscured AGN.

The *InfraRed Astronomical Satellite IRAS* has sampled the local Universe ($z < 0.2$) in the MIR/FIR band, discovering Ultra Luminous Infrared Galaxies (ULIGs: $L_{IR} > 10^{12} L_\odot$; Sanders & Mirabel 1996, Lonsdale, Farrah & Smith 2006) and first showing some evidence for their strong evolution (i.e. Hacking, Houck and Condon 1987, Lonsdale & Hacking 1989; Saunders et al. 1990).

Extragalactic source counts from different surveys over a wide flux range obtained with the *ISOCAM* instrument (Cesarsky et al. 1996) on board of the *Infrared Space Observatory* (*ISO*; Kessler et al. 1996) indicate that also IR sources less extreme than ULIGs (i.e. Luminous Infrared Galaxies; LIGs: $L_{IR} > 10^{11} L_\odot$) have evolved rapidly from $z \sim 0$ up to $z \sim 1.2$, significantly faster than deduced from optical surveys (i.e. Elbaz et al. 1999; Gruppioni et al. 2002; Pozzi et al. 2004).

The *Spitzer* Space Telescope (Werner et al. 2004) is now providing new insights into the IR population contributing to the CIRB, in particular in the *MIPS* 24-μm band, where the

extragalactic source counts (Marleau et al. 2004; Papovich et al. 2004) have confirmed the existence of the rapidly evolving dust-obscured population discovered by *ISOCAM*, detecting the higher-z analogues ($1 < z < 3$) of the *ISOCAM* galaxies. In particular, the deeper *MIPS* surveys are now able to resolve about 70% of the CIRB at 24 μm, with the bulk of this background originating in discrete sources at $z \lesssim 2$ (e.g. Papovich et al. 2004).

These results have stimulated the development of several evolutionary models for IR galaxies (i.e. Rowan-Robinson 2001; Franceschini et al. 2001; Chary & Elbaz 2001; Xu et al. 2003; Lagache, Dole & Puget 2003; Lagache et al. 2004; Pozzi et al., 2004; Gruppioni et al. 2005; Pearson 2005), aimed at reproducing the MIR source counts and the observed redshift distributions. All these models are more or less able to reproduce the observed *ISOCAM* 15 μm source counts, but none of them can provide an acceptable fit to the *MIPS* 24-μm counts without any "ad-hoc" changes. In particular, they tend to predict the characteristic turn-over of the differential 24-μm number counts at fluxes higher than observed. Even worse is the situation regarding the observed redshift distributions, both for *ISOCAM* and *MIPS* sources. Le Floc'h et al. (2005) and Pèrez-Gonzàlez et al. (2005), by studying the luminosity evolution of a sample of *MIPS* 24-μm sources in the Chandra Deep Field South (CDFS) up to $z = 1$ and in the range $1 < z < 3$ respectively, find that all the models considered in these works (Lagache et al. 2004, Chary et al. 2004, Gruppioni et al. 2005 and Pearson et al. 2005) fail in reproducing the differential counts at 24 μm in different redshift slices and the total z-distribution. We must note that most of the redshifts considered in these works are photometric and the analysed fields are relatively small, and can therefore be affected by cosmic variance. However, there seems to be a significant disagreement between all the evolutionary models existing in literature and the recent *Spitzer* data. Two main weaknesses are common to all these models:

1) They are based on very uncertain assumptions about the shape of the SED of MIR sources. In particular, they generally assume an invariant PAH emission and extrapolate few local SEDs to high redshifts and luminosities (L), either by keeping them fixed or artificially increasing their activity with luminosity (e.g. Chary & Elbaz 2001).

2) They severely underestimate, or even completely neglect (e.g. Lagache et al. 2003; Chary & Elbaz 2001), the AGN contribution in MIR sources (see Brand et al. 2006; Gruppioni et al. 2006). In fact, without MIR spectroscopic data or, if not available, without a complete SED characterisation, it is very difficult to disentangle star-forming galaxies from AGN (Genzel et al. 1998, Sajina et al. 2007). This is particularly true in cases where spectroscopic classification based on optical line diagnostics is impossible due to the absence of some of the required emission lines in the observed spectral range, or to the significant differential line extinction produced by dust, or to the lack

of spectroscopic data and deep X-ray coverage. Since different evolutionary models are applied to the two populations, the misidentification of AGN and star-forming galaxies introduces large uncertainties in the predicted source counts and backgrounds..

The crucial wavelength range (3-200 μm) covered by Spitzer with unprecedented sensitivities gives the opportunity to characterise for the first time the MIR/FIR spectral properties of large numbers of sources over a significant extent in redshift and to study their evolution with z and/or L, testing the model assumptions. In particular, thanks also to the extensive multi-wavelength coverage available in several areas of the sky, it is now possible to study the broad-band (from UV to FIR) spectral properties of the same sources responsible for the observed evolution in the MIR, thus constructing observational templates libraries over a large range of wavelengths.

In the Southern field of the European Large Area *ISO* Survey (ELAIS; Oliver et al. 2000; Rowan-Robinson et al. 2004), S1, an extensive multi-wavelength follow-up campaign has been performed during the past years. This field, initially selected for *ISO* observations at 7, 15 and 90 μm, is now one of the six areas covered by the *Spitzer* Wide-Area InfraRed Extragalactic Survey (SWIRE, Lonsdale et al. 2003) in all the *IRAC* and *MIPS* bands. In addition to *ISO* and *Spitzer* observations, the whole S1 field ($\sim$4 deg^2) has been deeply surveyed in the radio (*ATCA*; Gruppioni et al. 1999; Ciliegi et al., in preparation), in the optical (*R* band, *ESO/3.6-m*; La Franca et al. 2004) and in the near- and far-UV [Galaxy Evolution Explorer (*GALEX*); Burgarella et al. 2005]. The central square degree of S1 is covered by NIR (ESO/SOFI; Matute et al. in preparation) and optical (*ESO/WFI*; Berta et al. 2006) data, while $\sim$0.6 deg^2 have been observed in the X-rays (*Beppo-SAX*; Alexander et al. 2001 and *XMM-Newton*; Puccetti et al. 2006). Optical spectroscopic informations are available for $\sim$200 15-μm ISOCAM sources (*ESO/3.6-m*; La Franca et al. 2004) and for most of the *XMM* and some of the SWIRE-24μm sources having optical counterpart brighter than $R \approx 24$ (with *ESO/VIMOS*; Feruglio et al., 2008; La Franca et al., in preparation).

Due to its extensive multi-wavelength coverage and its large area extent, S1 is well suited to study in detail the broad-band SEDs of a statistically significant sample of infrared galaxies and AGN at intermediate redshifts ($z < 1.5$). To this purpose, we have selected the 203 extragalactic sources detected by *ISOCAM* at 15 μm ($S > 0.5$ mJy) in the S1 field (Lari et al. 2001) with $R < 23$, available spectroscopic redshift and classification (La Franca et al. 2004; La Franca et al. 2007). The same sample has previously been used to derive the first 15-μm luminosity function of galaxies (Pozzi et al. 2004) and AGN (Matute et al. 2002, 2006). The treatment of infrared/optical incompleteness of this sample for statistical purposes is described in detail by Gruppioni et al. (2002) and La Franca et al. (2004). The sample discussed here can be considered as the largest available spectroscopic sample of IR galaxies

and AGN at intermediate redshift, with such a high level of completeness (72%), allowing us for the first time to characterise the spectral properties of the sources responsible for the strong evolution observed in the MIR. Although large spectroscopic samples are available in fields observed by *Spitzer*, like the GOODS-CDFS (see Vanzella et al. 2005; 2006), the targets are not selected to be MIR sources, but optical/NIR objects responding to given colour criteria and likely to be at high redshifts. In the very near future large spectroscopic samples of MIR (24-μm) selected sources, either locally (i.e. in the FLS by Marleau et al. 2007) or at high redshift (i.e. in the COSMOS area) will be made available to the community, allowing studies similar to the one presented here, but at present our sample is unique to this purpose. Indeed most of our objects are LIGs, with MIR fluxes in the crucial range between the *IRAS* surveys (200 mJy) and the Deep *ISOCAM* Surveys (0.1 mJy; Elbaz et al. 1999), where MIR source counts start diverging from no-evolutionary expectations. Most of these objects (except for type 1 AGN) are in the redshift range $0.1 < z < 1.0$. We make use of all the available data, from FUV to FIR, to derive the SEDs of these sources and construct the first observational library of templates for MIR galaxies and AGN at intermediate z. To interpret the observed SEDs we perform a fit with several local template SEDs, representative of different classes of IR galaxies and AGN (Polletta et al. 2007), comparing the resulting SED classification with the spectroscopic one.

The present paper is structured as follows. In Section 2 we describe the reference sample. In Section 3 we present the multi-wavelength data-set and the observed SEDs, discussing the SED-fitting procedure and results. In Section 4 we compare the original spectroscopic classification with the SED classification. In Section 5 we present the revised 15-μm counts for AGN and galaxies, we discuss the results and present our conclusions.

Throughout the paper we adopt a cosmological model with $\Omega_m = 0.3$, $\Omega_\Lambda = 0.7$ and $H_0 = 70$ km s^{-1} Mpc^{-1}. The magnitudes discussed here are in the Vega system.

2. The Sample

Our reference sample is the Lari et al. (2001) catalogue of 462 sources selected at 15 μm (LW3 band) in the ELAIS Southern field S1 (centred at $\alpha(2000) = 00^h\ 34^m\ 44.4^s$, $\delta(2000) =$ -43° 28′ 12″, and covering about 2° × 2°). This sample, complete at the 5σ level, is the only *ISOCAM* sample covering the whole flux density range $0.5 - 150$ mJy, thus linking *IRAS* to the Deep ISOCAM Surveys (Elbaz et al. 1999). The source counts at 15 μm obtained from that catalogue sample the flux density region where observed counts start diverging from no evolution models, as discussed by Gruppioni et al. (2002). La Franca et al. (2004) presented R-band data for a highly reliable sub-sample of 406 out of the total 462 15-μm sources of the

Lari et al. (2001) catalogue. The R band data were obtained by an ESO imaging campaign with the *DFOSC* instrument mounted on the 1.5-m ESO/Danish telescope at La Silla (Chile), providing a reliable optical counterpart down to $R \sim 23$ for 317 of them, thus reaching 95% completeness level. Spectroscopic observations of the optical counterparts of the *ISOCAM* S1 sources were carried out at the *AAT/2dF*, ESO/Danish 1.5-m, 3.6-m and NTT telescopes (La Franca et al. 2004), providing a secure spectroscopic identification for 290 *ISOCAM* sources (72% of the whole highly reliable ELAIS-S1 sample). La Franca et al. (2004) have classified 199 of the spectroscopically identified sources as extragalactic objects (25 type 1 AGN, 23 type 2 AGN, 9 liners, 32 starburst galaxies, 100 Hα emitter galaxies, 3 early type galaxies, 7 unclassified, but with measured redshift), the remainder 91 as stars. Details about the identification completeness of the extragalactic sample for statistical uses are given in La Franca et al. (2004). These 199 extragalactic objects with measured redshift are the same objects previously used for the statistical analysis of the evolution of galaxies and AGN by Pozzi et al. (2004) and Matute et al. (2002, 2006) respectively. With respect to the La Franca et al. (2004) catalogue, two more 15 μm sources were spectroscopically identified through VIMOS-VLT observations (La Franca et al. 2007): ELAISC15_J003317−431706 is a $R = 24.3$ galaxy showing [OII] emission at redshift 0.689, while ELAISC15_J003447−432447 is an AGN2 at redshift 1.076. Moreover, we derived redshifts for two additional 15 μm sources: for ELAISC15_J003915−430426 we found a z value of 0.013 in the NED database, while for ELAISC15_J003545−431833 we were able to measure z through a more accurate reduction of the spectrum. Three sources with previously poor quality spectra changed their spectroscopic classification after having been re-observed with VIMOS at ESO-VLT (La Franca et al. 2007): ELAISC15_J003330−431553, which was wrongly classified as a starburst galaxy at $z = 0.473$, showed broad CIII and MgII emission at $z = 2.170$ typical of AGN1 activity; ELAISC15_J003603−433155, which was classified as AGN2, showed a broad MgII emission typical of AGN1 activity; and ELAISC15_J003622−432826, which was classified as a starburst galaxy, showed a clear [OIII]/Hβ ratio typical of AGN2 activity.

In summary, we have considered 203 extragalactic sources selected at 15 μm with $R < 23$, spectroscopic redshift and multi-band photometry.

3.   The SEDs

3.1.   The Multi-Wavelength Data-Set

The objects we focus on cover the redshift range $0.01 - 3.09$ ($0.01 - 1.30$ if excluding type 1 AGN) and more than two orders of magnitude in 15-μm flux ($0.5 - 60$ mJy). The multi-band SEDs for these sources have been constructed by looking for counterparts in all the

multi-wavelength catalogues from far-UV to FIR available in the ELAIS-S1 field. Given for granted the optical R-band/spectroscopic association performed by La Franca et al. (2004), we have searched for associations in the *GALEX* Deep Imaging Survey (DIS), ESIS, J, Ks and SWIRE catalogues. The cross-correlation radii between the 15-μm or optical positions and the different matching catalogues positions have been chosen equal to the value above which spurious associations start dominating (i.e. Hook et al. 1998).

The ultraviolet Galaxy Evolution Explorer (*GALEX*, Martin et al. 2005) Deep Imaging Survey (DIS) is observing $\sim$100 deg^2 in 12 different areas of the sky, including ELAIS-S1 (Burgarella et al. 2005). Twelve ELAIS-S1 *GALEX* tiles are already available to the public as part of the second data release (GR2). The exposure times for these tiles vary from $\sim$3000 to $\sim$50000 sec. The photometric catalogues in the far-UV (FUV; 1530 Å) and near-UV (NUV; 2310 Å) have been cross-correlated with the optical positions of the *ISOCAM* source counterparts, with a matching radius of 3 arcsec. Then all the possible UV counterparts have been visually inspected on the GALEX images, in order to reject spurious associations. We found 176 likely associations with the NUV catalogue, 169 of which are also in the FUV one.

The *ESO-Spitzer* Imaging Extragalactic Survey (ESIS; Berta et al. 2006) has covered the central 1.5 deg^2 of ELAIS-S1 with WFI/2.2-m deep observations in the B, V and R bands, reaching 95% completeness at $B, V \sim$ 25 and $R \sim$24.5. The cross-correlation between the original optical positions and the ESIS positions (within 2 arcsec) have produced a good match for 90 sources (those falling in the area covered by ESIS), thus providing additional optical (B, V) magnitudes for about 45% of the 203 *ISOCAM* sources. In the area not covered by ESIS, R magnitudes from the La Franca et al. (2004) catalogue and b_J magnitudes from APM survey ($\sim$90% complete to $b_J = 20.5$; Maddox et al. 1990) have been used.

The central square degree of the ELAIS-S1 area (S1-5) was the target of NIR J and Ks imaging with NTT/SOFI, reaching $J \simeq$21 and $Ks \simeq$20 (Vega)[1] (Matute et al., in preparation). The optical positions of the 15-μm source counterparts have been cross-correlated with the NIR catalogue ones, using a matching radius of 2 arcsec. Thirty unique NIR counterparts have been found in the central square degree of ELAIS-S1, while additional NIR data from the Two Micron All Sky Survey (2MASS; Jarrett et al. 2000) are available over the whole *ISO* area, providing 110 matches (10 of which are in common with the S1-Ks ones). In total we found Ks-band magnitudes for 130 and J-band magnitudes for 30 out of the 203 15-μm sources.

The *Spitzer*/SWIRE observations in ELAIS-S1 cover the whole *ISO* region and a total

---

[1]as part of the ESO Large Programme 170.A-0143, P.I. A. Cimatti

sky area of $\sim$7 deg^2 in all the *IRAC* and *MIPS* bands, reaching 5σ sensitivities of 4.1, 8.5, 48.2, 53.0, 256.0, 26$\times$10^3 and 166$\times$10^3 μJy in the 3.6, 4.5, 5.8, 8.0, 24, 70 and 160 μm channels respectively (Lonsdale et al. 2004). The SWIRE data in ELAIS-S1 have been released to the community in autumn 2005 (Data Release 3, DR3) through the query building GATOR at the NASA/Infrared Science Archive (`http://irsa.ipac.caltech.edu/applications/Gator/`). However, to the purposes of this work, we had access to the SWIRE working catalogues, which contain all of the sources in the public catalogue, but reach deeper flux densities. Details about the SWIRE data reduction, that was carried out by the Spitzer Science Center and SWIRE team, can be found in the Data Release paper (Surace et al. 2005[2]). For the *IRAC* fluxes and positions we used the band-merged working catalogue, consisting of *IRAC* and *MIPS*-24 μm fluxes associated with each other. While the public catalogue is a 3.6-μm based one, requiring detections at 3.6 and 4.5 μm above specific SNR thresholds (10 at 3.6 μm and 5 at 4.5 μm), the working catalogue contains all detections, at any signal-to-noise ratios and even if a source is detected only in one *IRAC* band. For the 24-, 70- and 160-μm fluxes and positions, we used the single-band only catalogues, which contain all the sources detected only in the *MIPS* waveband in question. The *IRAC* positional accuracy is about 0.2″–0.4″ in all bands, while the *MIPS* ones are $\sim$1″, 4″ and 8″ at 24, 70 and 160 μm respectively. Fixed aperture photometry is used for point-like objects, corrected for aperture losses (we have considered the SWIRE "aperture2" (1.9 arcsec in radius) for both *IRAC* and *MIPS*), while "ad-hoc" aperture photometry (i.e. as large as needed to recover the whole flux of very extended sources) has been performed by us directly on images for the extended sources, for which even the SExtractor's Kron fluxes (those suggested for extended sources) are found to underestimate the total flux densities (up to a factor of $\sim$2 at 24 μm). For the match with the *IRAC* band-merged catalogue we have considered the optical positions, searching for counterparts within a radius of 3 arcsec, while for match with the *MIPS* catalogues we have considered the *ISOCAM* positions with searching radii of 5, 10 and 20 arcsec at 24, 70 and 160 μm respectively. All but one of the 203 15-μm sources are detected in at least two *IRAC* bands (most in all 4 bands), while 200 are detected at 24 μm, 110 at 70 μm and 59 at 160 μm. The matches with 24-, 70- and 160-μm sources have been visually inspected to be sure they were not mismatches. From the visual inspection of the *MIPS* images we have found clear detections for 43 and 45 additional sources at 70- and 160-μm respectively. However, we have chosen not to derive flux densities for these sources, considering in this work only those included in the SWIRE catalogues.

In Table 1 we report the multi-wavelength informations available for all the 203 15-μm sources. The source name from the Lari et al. (2001) catalogue is reported in the first

---

[2]also `http://data.spitzer.caltech.edu/popular/swire/20050603_enhanced_v1/Documents/SWIRE2_doc_083105.pd`

column, while the flux density (in μJy) in all bands, from FUV to FIR, the redshift and the total infrared luminosity (obtained by integrating the best-fitting SED in the range 8 – 1000 μm) are reported in the following columns. In the last two columns the spectroscopic and SED-fitting classifications (see Section 4) are presented. In case of no detection we have quoted a 3σ upper limit, while $-$ means "no data coverage".

3.2. The Template Library

We have made use of all the available data, from FUV to FIR, to derive the SEDs of these 203 sources and construct the first highly complete observational sample of SEDs for MIR galaxies and AGN at intermediate z to be used for statistical purposes (i.e. luminosity function). To interpret and classify the observed SEDs, we have performed a fit with several local template SEDs, representative of different classes of IR galaxies and AGN (including 3 Ellipticals of different ages, 1 lenticular, 7 Spirals, 3 Starbursts, 3 QSOs, 1 reddened QSO, Seyfert 1, 1.8 and 2 and 2 ULIRGs, containing both a starburst and an AGN component, in the wavelength range between 0.1 and 1000 μm (Polletta et al. 2007), appropriately redshifted to the rest frame. The full library of galaxy and AGN templates (excluding the three ellipticals since none of our sources could be fitted by any of them) is shown in Fig. 1. The elliptical, spiral and starburst templates were generated with the GRASIL code (Silva et al. 1998). The spiral templates range from early to late types (S0-Sdm), the starburst templates correspond to the SEDs of NGC 6090, M 82 and Arp 220. Templates of moderately luminous AGN, representing Seyfert 1.8 and Seyfert 2 galaxies, were obtained by combining models and data from a large sample of Seyfert galaxies. The AGN templates include three templates representing optically-selected QSOs with different values of IR/optical flux ratios (QSO, QSO_high, and QSO_low) and one reddened QSO (red_QSO). The composite (AGN+SB) templates are empirical templates created to fit the SEDs of the heavily obscured BAL QSO Mrk 231 (Berta 2005) and the Seyfert 2 galaxy IRAS 19254$-$7245 South (Berta et al. 2003). These objects contain a powerful starburst component, mainly responsible for their FIR emission, and an AGN component that contributes to the MIR (Farrah et al. 2003). With respect to existing template libraries derived from empirical SEDs (Coleman et al. 1980) or from models (Bruzual 2003; Fioc et al. 1997; Silva et al. 1998; Devriendt 1999), this library has a broader wavelength coverage and variety of spectral types. Examples of application of this library to various types of SWIRE sources can be found in Lonsdale et al. (2004), Franceschini et al. (2005), Hatziminaoglou et al. (2005), Jarrett et al. (2006), Polletta et al. (2006), Weedman et al. (2006), Tajer et al. (2007), Polletta et al. (2007).

To avoid biasing the results in favour of a small subset of templates, we adopt the full

library of Polletta et al. (2007) to fit the SEDs. Although some templates are obtained from modelling the SEDs of Ultra-Luminous objects (ULIGs, $L_{IR} > 10^{12}L_\odot$: e.g. Mrk 231, I19254 and Arp 220), they are kept in the library since they well represent a large fraction of the Spitzer population at several flux and luminosity levels (see e.g. Franceschini et al. 2005, Polletta et al. 2006, 2007, Alonso-Herrero et al. 2006).

3.3. The Fitting Method

The SEDs of our sources are fitted using an automated fitting routine contained in the *Le PHARE* software (by Arnouts & Ilbert, available at http://www.lam.oamp.fr/people/arnouts/LE_PHARE.html), offering the possibility of using any template library and filters set. *Le PHARE* (PHotometric Analysis for Redshift Estimations; Ilbert et al. 2006) is a publicly available set of fortran programs aiming at computing photometric redshifts through the best-fitting SED analysis. The program is based on a simple χ^2 fitting method between the expected magnitudes and an observed photometric catalogue.

Since we already know the spectroscopic redshift of our galaxies, we have fixed z and have used *Le PHARE* only to obtain the best-fitting SED through a comparison with the template SEDs. No extinction was added to the templates, since some of them are already intrinsically extinct. Note that by using a spectroscopically complete sample we are able to avoid all the uncertainties due to the photometric redshift measurements, which greatly increase the degeneracy in the SED-fitting procedure. Moreover, for the first time we can compare the results from optical spectroscopy with the broad-band SED shape of a statistically significant sample of MIR galaxies and AGN.

We make the basic assumption that the SED shapes seen at low redshifts can also well represent the higher redshift objects. At the end of our procedure we would be able to verify this assumption. The template library used to fit our data contains a finite number of SEDs (21), representative of given classes of local infrared objects, which do not vary with continuity from one class to another (there are large gaps in the parameter space). Therefore, the quality of the fit depends not only on the photometric errors, but also on the template SED uncertainties. For this reason, in our fitting procedure, in addition to the photometric errors on data, we need to take into account also the uncertainties due to the template SEDs "discretization". To estimate and consider the total uncertainty on both the photometric data and the template SEDs, we have proceeded as follows. First, we have increased all the formal catalogue errors (probably too small) by a reasonable given amount, going from 5% in the UV, and optical bands up to $\sim$15% in the *MIPS* bands. We have run *Le Phare* on all the sources, obtaining a first "estimate" of the best-fitting SED classification.

We have then computed the distributions of the $(S_{object} - S_{template})_{band}/(\sigma_{object})_{band}$ values in each of the considered photometric band (where S_{object} and σ_{object} are the flux density and the relative error of the source, and $S_{template}$ the flux of the template in the considered band), iteratively increasing the photometric errors until we have obtained a Gaussian distribution with $\sigma \simeq 1$. This corresponds to reduced χ^2 distributions peaked around 1 (as should be in case of good fit). The enlarged relative errors ($\sigma_{object}/S_{object}$) obtained in this way go, on average, from $\sim$12–15% in the optical/NIR/$IRAC$ bands up to $\sim$20% in the $MIPS$ $bands$. With the new (significantly larger) photometric uncertainties, which now take into account also the additional uncertainties induced by the template SED discretization, we have run Le $PHARE$ on our sources for the second time, obtaining what we have taken as the final SED-fitting results.

3.4. The SED-Fitting Results

In figure 2 examples of data overlying the best-fitting template SEDs are shown for most of the templates reproducing our data (the original library contains 21 SEDs, but none of our sources could be fitted by any of the 3 elliptical galaxy templates). We find that 83 sources (41%) are reproduced by a galaxy template SED (4 S0, 3 Sa, 16 Sb, 27 Sc, 18 Sd, 15 Sdm), 13 (6.5%) with a starburst template SED (1 Arp 220, 5 M 82, 7 NGC 6090), 72 (35%) with a type 2 AGN template SED (52 Seyfert 2, 15 Seyfert 1.8, 5 red QSO), 11 (5.5%) with a ULIG composite SED (9 Markarian 231, 2 I19254) and 24 (12%) with a type 1 AGN SED (3 Seyfert 1, 6 QSO, 13 high IR/optical flux ratio QSO, 2 low IR/optical flux ratio QSO). Therefore, with our broad-band SED-fitting method we find AGN activity in 52.5% of our MIR selected sample.

We note that the distributions of the final $log_{10}(S_{object}/S_{template})$ values in some bands and for some SED classes are centred on values slightly different from 0. These offsets, which are different in the different bands and for the different best-fitting SED classes (i.e. for the QSO class the larger offsets are observed at 70 and 160 μm, while for the galaxy class the larger offsets are observed in the B, J, K, 15-μm and 24-μm bands; see Fig. 3), are interpreted as the average values we should add to the template SEDs to better reproduce the data ensemble of MIR sources. In Fig. 3 we show the rest-frame SEDs (dots) of 15-μm sources belonging to the different "broad" SED classes (AGN1, ULIG, AGN2, Starburst and Spiral galaxy), compared to the most frequent best-fit template SED of that class (i.e. "QSO" for AGN1, "Seyfert 2" for AGN2, "Mrk 231" for ULIG, "NGC 6090" for Starbust, "Sc" for Spiral), all normalised to the Ks-band flux density. The white triangles represent the average values that the templates should have in the different rest-frame bands to better reproduce

the bulk of our sources, while the grey-shaded areas represent their relative uncertainty region corresponding to $\pm 1\sigma$ of the expected values. From this check we can conclude that, on average, the template SEDs of the Polletta et al. (2007) library modelled on local galaxies and AGN are able to reproduce also most of the MIR selected sources at intermediate redshifts, though some of the local templates should be slightly modified in some wave-bands to get a better agreement with the bulk of the observed data.

In order to estimate the reliability of the SED classification, we compared the classification and χ^2 obtained by the two best solutions of each fit: the primary (corresponding to the minimum χ^2 value, χ^2_{best}) and the secondary solutions (χ^2_{2nd}). We find that the primary solutions of our photometric analysis are quite stable within uncertainties. In fact, for the majority of our sources (92%) the χ^2_{best} values are within the 90% probability threshold ($\chi^2_{90\%} = 21.07$ for the case of 14 degrees of freedom). In most cases the secondary solution belongs to the same "broad" SED class of the primary (i.e. AGN or galaxy, containing all the type 1's, type 2's and ULIG templates and all the galaxy and starburst templates, respectively) and only for 23 objects (11%) it belongs to a different class, with a χ^2_{2nd} lower than the $\chi^2_{90\%}$ threshold. In all the other cases, if the primary and secondary solutions correspond to different SED classes, the secondary solutions have a low probability of being acceptable ($\chi^2_{2nd} > \chi^2_{90\%}$). The 16 sources (8%) with a statistically bad primary solution ($\chi^2_{best} > \chi^2_{90\%}$) have, in a few cases, some evident photometric errors in one or more bands (mainly in the J, K' ones). In all the remaining cases, the bad fit is due to an observed SED flatter than the best-fitting template in the MIR domain, thus implying the need of a template SED (missing in our library) intermediate between the power-law and the Seyfert 2/1.8 ones, where the AGN is not dominant as in the type 1 template case (power-law), but its contribution is higher than in the Seyfert 2 template case.

4. Spectroscopic versus SED Classification

We have compared the results of our SED-fitting procedure with the results obtained from the optical spectroscopy. In Table 2 we show for each spectroscopic class the number of sources which are best fitted by the various SED templates and vice-versa. The reported percentages are the fractions of sources of a given spectroscopic classification fitted by the various template SEDs. The spectroscopic type 1 (broad line) AGN are all fitted by AGN template SEDs, and therefore the agreement between the two classifications for type 1 AGN is very good (the only three objects fitted by a type 2 AGN template are indeed fitted by a Seyfert 1.8 template). However, the agreement is not equally good for the spectroscopic type 2 AGN (+ LINERs) and galaxies: 56% of the AGN2+LINER sample is fitted by a type

2 AGN template and another 19% is fitted by type 1 AGN or composite (AGN+starburst) templates, but ∼25% do show a galaxy SED. Also for the majority (63%) of the spectroscopic normal galaxies the two classifications agree (another 3% is fitted by a starburst template), but there is a significant fraction (34%) fitted by AGN templates (mostly type 2's). For the spectroscopic starbursts the fraction of sources classified as AGN by the SED fitting is even higher, 53%. The small number of spectroscopically unclassified sources is fitted for the 40% by AGN and for the 60% by galaxy templates. Therefore, we can conclude that the SED-fitting technique applied to our MIR selected sample is able to identify AGN activity in ∼40% of sources spectroscopically unclassified, in ∼34% of sources spectroscopically classified as galaxies, in ∼53% of spectroscopic starbursts, in 75% of type 2 AGN or LINERs, and in 100% of type 1 AGN. The main result of this comparison is that, although for many sources the spectroscopic classification is in agreement with the classification resulting from the SED-fitting method, the broad-band SED analysis is able to find AGN activity in a higher fraction of MIR sources (∼53%) than the optical line diagnostic techniques (∼29%). On the other hand, a small number (14%) of the spectroscopically classified AGN are classified as galaxies by the SED fitting.

For comparison, we cite the recent results of Polletta et al. (2007), who, using a sample of X-ray selected AGN with available spectroscopic classification and a similar fitting method as applied to our sample, find that 82% of the X-ray selected AGNs are classified as AGN by the SED-based classification method, compared to 78% by the spectroscopic classification. However, the SED and the spectroscopic classification agree only in 53% of the cases: the SED method and the spectroscopic classification for X-ray sources are consistent for all type 1 AGN, but for only 29% of type 2 AGN and 33% of AGN with galaxy spectra.

The more evident change between the spectroscopic and SED classifications in our sample is due to the fact that several sources optically classified as normal or starburst galaxies do show a Seyfert 2/Seyfert 1.8-like SED, or possibly a composite (starburst+AGN) SED. Therefore, the total fraction of type 2 AGN increases from 15.5% (spectroscopic) to 36% (SED-fitting), while that of galaxies powered by star-formation (normal+starburst) decreases from 70% (spectroscopic) to 48% (SED-fitting). In addition, we have 4% of composite (AGN+starburst) SEDs that were not considered as spectroscopic class.

As a partial explanation of these discrepancies, we note that many of the sources spectroscopically classified as normal galaxies do not have enough lines in their optical spectra to be properly classified according to the standard line ratios diagnostics (i.e. Tresse et al. 1996). In fact, many of them have only $H\alpha$ and/or $[OII]$ in emission and therefore the spectroscopic classification might be misleading. However, in all the cases where the classification changed from spectroscopy to SED-fitting, the spectra do either show no AGN

emission lines (e.g. [OIII]) at all, or lower than those due to star-formation, making them clearly classified as galaxy (normal or starburst) through the diagnostics diagrams. In any case, the SED-fitting procedure seems to find more AGN than the optical spectral lines classification. One possible reason is that in most of these objects the AGN dominates the energetic output only in the MIR. Indeed, most of the sources in our sample with galaxy spectroscopic classification and SED reproduced by a Seyfert 2/1.8 template could be fitted by a normal galaxy in the optical/NIR part of their spectra, but not in the MIR (in particular in the 3–8 μm range), where the data are too flat to be reproduced by a normal/starburst galaxy SED and therefore require the presence of a low-luminosity AGN. The AGN shows up just in the range where the host galaxy SED has a minimum, due to the junction between the stellar photospheric emission (dominating the optical/NIR) and the dust component (starting dominating at $\lambda > 5\mu$m; see e.g. the late-type spirals and starburst templates in Fig. 1), which is also the range where the hot dust heated by an AGN is expected to start increasing towards the peak. In case an AGN component is present with a NIR luminosity similar to that of the host galaxy, emission from hot dust heated by the AGN contributes to the NIR/MIR filling up the dip observed in star-forming galaxies and producing a flat NIR/MIR spectrum (see e.g. the Seyfert templates in Figure 1). This is consistent with the results about X-ray selected obscured AGN, which are known to be "elusive" in their optical spectra due to host galaxy dilution or heavy dust and gas obscuration or both (i.e. see Fiore et al. 2003; Maiolino et al. 2006; Tajer et al. 2007; Caccianiga et al. 2007; Civano et al. 2007; Cocchia et al. 2007). Unfortunately, a check with the X-ray luminosity for our "elusive" AGN is inconclusive for our purposes, since the XMM observations cover only a small portion of the field (15%).

In order to visualise what discussed above and look at the average properties (in terms of redshift and rest-frame luminosity) of the different SED classes, in Fig. 4 we show the redshift (in logarithmic scale) and the $\log(L_{15\mu m})$ distributions for the different SED classes to which our sources belong. We notice a clear trend of increasing 15-μm luminosity (and z) from early-type (S0, Sa) to later-type (Sd, starburst) SEDs. Type-2 AGN are spread over almost the entire range of $L_{15\mu m}$ ($\sim 10^9 - 10^{12}$ $L_\odot$, except two $z > 2$ objects at $L_{15\mu m} > 10^{13}$ $L_\odot$) and over a large redshift range (0.05< z <3), while type 1's occupy the region of higher luminosities ($L_{15\mu m} > 10^{10}$ $L_\odot$) and redshifts (most of them are at $0.5 < z < 3$). The different spectroscopic classifications have been highlighted by filling the relative distributions with different patterns, as shown in the legend within the plot.

Although very uncertain, since the templates often do not fit well the 70 and 160 μm data, the total IR luminosities (L_{IR}) have been computed by integrating the best-fitting template SEDs between 8 and 1000 μm. Most of the starburst galaxies and some of the type 2 AGN are in the ULIG luminosity range ($L_{IR} > 10^{12}$ $L_\odot$), with the remainder in these two

classes in the LIG range ($10^{11} < L_{IR} < 10^{12}$ L$_\odot$). The majority of normal galaxies have $L_{IR} < 10^{11}$ L$_\odot$, with just some in the LIG range. All the type 1 AGN are in the ULIG range, with few even in the Hyper-LIG (HyLIG) range ($L_{IR} > 10^{13}$ L$_\odot$), where all the composite AGN are indeed.

5.   Discussion and Conclusions

We have derived the broad-band (from FUV to FIR) SEDs for the largest available highly complete (72%) sample of intermediate-z MIR selected galaxies and AGN with spectroscopic identification and redshift. The majority of these objects are at $0.1 < z < 1.3$ and in the flux density range where strong evolution is observed in the counts of MIR sources. Their broad-band SED characterisation is therefore fundamental to understand the nature of sources responsible for the observed evolution. Based on the SED-fitting technique we have classified the MIR sources, identifying AGN signatures in about 53% of them. This fraction is significantly higher than that derived from optical spectroscopy ($\sim$29%) and is due principally to the identification of type 2 AGN activity in objects spectroscopically classified as galaxies. This might be caused, at least in part, by host galaxy dilution in the optical, similarly to what is observed for obscured AGN selected in X-ray. It is likely that in most of our objects where the AGN luminosity in the optical band is fainter than that of the host galaxy, the AGN dominates the energetic output only in the MIR, showing up just in the range where the host galaxy SED has a minimum, while the hot dust heated by the AGN is expected to start peaking.

We note that the fraction of MIR sources with an "elusive" AGN derived in this work is in agreement with recent results from MIR spectroscopy (with *Spitzer-IRS*) of local star-forming galaxies from the *Spitzer*-SINGS sample by Smith et al. (2007), who find that a high fraction ($\sim$50%) of local galaxies do harbour low-luminosity AGN (LINER or Seyfert types). These low-luminosity AGN, contrarily to the luminous ones which completely destroy PAH grains, are able to excite the PAHs and to modify the emitting grain distribution, thus providing unusual PAH spectra with very weak or absent 6.2 μm, 7.7 μm and 8.6 μm bands, suppressed in strength by up to a factor of 10. An indication of the presence of such weak AGN systems, which are found to shift power from the short to the long wavelength PAHs, can be revealed, for example, by the strength ratio between the PAH features at 7.7 μm and at 11.3 μm (Smith et al. 2007). Therefore, the definitive confirmation of the presence of weak AGN systems in our intermediate-z MIR dusty galaxies, at present, could be obtained only through *IRS* spectroscopy, allowing to test with line ratios their SED shape indications.

Given the new percentages of AGN, we have updated the relative fractions of AGN

and galaxies contributing to the observed 15-μm source counts. Although the results of our work might still be affected, at some level, by photometric errors in the data and by some degrees of degeneracy in the template SEDs, the analysis of the photometric errors and the agreement between the primary and secondary solutions in the vast majority of the cases make us confident that the majority of the SED-classified AGN are reliable. For coherence with the previous classification and source counts (see La Franca et al. 2004 and considerations therein) and to avoid biasing towards AGN, we have treated all the sources without spectroscopic redshift as galaxies. In fact, a spectroscopic sample 72% complete can be biased towards AGN since the large majority of the spectroscopically unidentified objects have 15-μm flux densities fainter than 1 mJy. Galaxies dominate over AGN in this range of flux and it is therefore likely that most of the unidentified objects are galaxies. On the other hand, since we know that optical spectroscopy can miss AGN signatures, we can take the fraction of spectroscopic AGN (used for deriving the AGN LF at 15 μm by Matute et al. 2006) as a lower limit. In Fig. 5 we show the fractions of AGN as function of 15-μm flux obtained by considering the spectroscopic classification (dashed line; from Matute et al. 2006) and the SED classification (filled circles with error-bars; this work). Other recent works (Brand et al. 2006; Treister et al. 2006), though based on different diagnostics (e.g. the 24 μm to 8 μm flux ratio or X-ray detection), estimate lower limits to the AGN contribution in MIR surveys significantly higher than those predicted by Matute et al. (2006) and in very good agreement with the fractions derived in this paper (see Fig. 5, where the Brand et al. 2006 and Treister et al. 2006 results are reported for comparison, with the 24-μm flux densities converted to 15 μm by using the opportune 24/15 μm ratio as function of flux as computed by Gruppioni et al. 2005). Such results might have a significant impact on the interpretation of galaxy and AGN evolution and on the physics of the MIR selected objects, so far often erroneously assumed to be all starburst galaxies in many models. In fact, all the existing models of galaxy and AGN evolution in the IR should be revised by taking into account the higher fraction of AGN dominating in the MIR wave-range.

By comparing the AGN fraction derived by our SED-fitting analysis to the "lower-limit" coming from the spectroscopic classification, we can determine how the relative source counts of galaxies and AGN (and consequently the relative evolutionary models) should change according to the new values. To this purpose, in Fig. 6 we have plotted the extragalactic source counts at 15 μm in the S1 field (Gruppioni et al. 2002) with the relative contribution of galaxies and AGN computed according to the previous ($left$) and new ($right$) determination of AGN fractions. The difference between the two is small at bright fluxes, but the SED fitting method finds more and more AGN going to fainter fluxes. The galaxy population now dominates below $\sim$3 mJy (previously 6–7 mJy), although now the AGN counts are only a factor of 2 lower even at the lower flux densities. For comparison, we have also shown the

results of a recent work by La Franca et al. (2007), who updated the AGN source counts at 15 μm on the basis of X-ray band (*XMM*) observations (Puccetti et al. 2006) on the central 0.6 deg^2 of ELAIS-S1. By classifying as AGN all the MIR sources with an unabsorbed 2-10 keV X-ray luminosity $> 10^{42}$ erg s^{-1}, the authors find that at least 13% of the previously classified galaxies on optical basis (by La Franca et al. 2004) do harbour an AGN, therefore concluding that $> 24\%$ of the 15-μm sources with flux density > 0.6 mJy are AGN. The AGN source counts at 15 μm updated by La Franca et al. (2007) and plotted in Fig. 6 as dot-dot-dashed line are indeed significantly higher that those based on optical classification, and in better agreement with (although somewhat lower than) the AGN counts derived in this work. The higher efficiency of the SED-fitting technique with respect to X-ray luminosities in detecting AGN activity, in this specific case, might be partially due to the fact that *XMM* observations in S1 are not deep enough (S(2–10keV) $= 2 \times 10^{-15}$ erg cm^{-2} s^{-1}) to detect (and thus allow conclusive results for) all (most of) our sources. Moreover, it is known that even the deepest X-ray surveys fail in detecting highly obscured (i.e. Compton thick: $N_H > 10^{24} cm^{-2}$) AGN, while sensitive measurements in the IR range, and in particular SED studies in the NIR/MIR range, provide a unique and efficient opportunity to recover the fraction of obscured or "elusive" AGN not identified in X-ray surveys (Alonso-Herrero et al. 2006; Fiore et al. 2008; Martinez-Sansigre et al. 2007; Daddi et al. 2007).

We have compared our results to those of Hickox et al. (2007), though the sample selected by those authors is an *IRAC* selected one fulfilling also additional selection criteria (i.e. detection in all the *IRAC* bands and in the *R* band, *IRAC* colours falling in the Stern et al. 2005 AGN selection region, spec- or photo-z >0.7), finding that according to the Hickox et al. criteria just a few of our AGN can be considered "obscured". In fact, very few of our AGN do fall above the $R - [4.5]$=6.1 separation boundary considered by Hickox et al. (2007) to divide "obscured" from "unobscured" AGN. All our type 1 and most of type 2 are below that boundary, while most of the composite AGN are above. This would imply that most of our composite AGN are "obscured" and all our type 1 and most of our type 2 AGN are "unobscured". The cumulative redshift distribution of our $z > 0.7$ AGN is in good agreement with that derived by Hickox et al. (2007), up to $z = 1.2 - 1.3$. Above $z = 1.3$ there are just few sources in our sample, due to our relatively bright 15-μm and R-band selection, therefore we can consider our AGN (in particular type 2) sample complete only up to $z = 1.3$.

The results of this work will be very useful for updating all the models aimed at interpreting the deep infrared survey data and, in particular, for constraining the nature and the role of dust-obscured systems in the intermediate/high-redshift Universe. The main changes to the actual evolutionary models for IR galaxies and AGN would consist in better defined evolutionary source classes (and SEDs) and in updated evolutions for the different classes.

In particular, referring to the specific case of the Pozzi et al. (2004) and Matute et al. (2006) models, which are based on the same sample considered here, although star-forming galaxies are still the dominant class at low flux densities, their evolution should be lower than that derived by Pozzi et al. (2004). Similarly, the AGN (mainly type 2's) should evolve more rapidly (and probably both in luminosity and density) than derived by Matute et al. (2006), similarly to star-forming galaxies. In fact, the higher fraction of AGN in infrared surveys than found through optical spectroscopy is a result common to different works (i.e. Brand et al. 2006; Treister et al. 2006) and applies mainly to type 2 AGN. Type 1 AGN are in fact easier to identify in optical, due to their broad lines, thus most (all) of them are classified from their optical spectra. Type 2 AGN are more "elusive" and difficult to reveal in the optical. Therefore, the higher fraction of IR AGN is mainly due to the unveiling of type 2 AGN previously erroneously classified as galaxies. For this reason, the starburst galaxies, to whom all the evolution observed in the MIR was commonly attributed, are probably in a smaller number than formerly believed and part of their evolution should be ascribed to type 2 AGN. This is also evident from the right panel of Fig. 6, where the revised AGN source counts increase towards fainter fluxes with a slope similar to (though slightly lower than) that of galaxies, while, according with the results based on optical spectroscopy (left panel), the AGN were rapidly converging towards the lower flux densities.

Finally, instead of considering non-evolving normal galaxies (and therefore ascribing all the evolution to starburst galaxies), it would be more appropriate to consider galaxy SEDs evolving with z (and/or L) from early-type to late-type (and to starburst), as suggested by the results shown in Fig. 4, and eventually different evolutions for different luminosity intervals. The revision of evolutionary models for IR sources based on the results presented here is beyond the aims of this work and will be treated in a forthcoming paper (Gruppioni et al., in preparation).

To summarise, in this paper through the broad-band SED analysis of the largest available highly (72%) complete spectroscopic sample of MIR selected galaxies and AGN at intermediate z, we have:

- verified the assumption that local template SEDs are able to reproduce also most of the MIR-selected galaxies and AGN at $0.1 < z < 1.3$;

- found AGN activity in a significantly higher fraction of sources ($\sim$53%) than derived from optical spectroscopy ($\sim$29%);

- derived new relative fractions of AGN and galaxies contributing to the observed MIR source counts, with AGN going from $\sim$10–20% of the MIR population at $S_{15} <$0.6 mJy up to $\sim 90 - 100\%$ at $S_{15} > 10$ mJy;

- computed new source counts in the MIR, with the AGN counts (especially type 2's) now increasing with a slope similar to that of galaxies. This result is likely to imply different evolutionary rates than formerly considered by the present models (i.e. lower rates for starburst galaxies and higher rates for type 2 AGN).

REFERENCES

Alonso-Herrero, A., et al. 2006, ApJ, 640, 167

Berta, S. 2005, Ph.D. Thesis, University of Padua, Italy

Berta, S., et al. 2006, A&A, 451, 881

Berta, S., Fritz, J., Franceschini, A., Bressan, A., & Pernechele, C. 2003, A&A, 403, 119

Brand, K., et al. 2006, ApJ, 644, 143

Brandt, W. N., & Hasinger, G. 2005, ARA&A, 43, 827

Bruzual, A. G. & Charlot, S. 2003, MNRAS, 344, 1000

Burgarella, D., et al. 2005, ApJ, 619, L63

Caccianiga, A., Severgnini, P., Della Ceca, R., Maccacaro, T., Carrera, F.J., Page, M.J., 2007, A&A, 470, 557

Cesarsky, C.J., Abergel, A., Agnèsel P., et al. 1996, A&A, 315, L32

Chary, R., & Elbaz, D. 2001, ApJ, 556, 562

Chary, R., et al. 2004, ApJS, 154, 80

Civano, F., et al. 2007, A&A, 476, 1223

Cocchia, F., et al. 2007, A&A 466, 31

Coleman, G. D., Wu, C.-C., & Weedman, D. W. 1980, ApJS, 43, 393

Daddi, E., et al. 2007, ApJ, 670, 173

Devriendt, J. E. G., Guiderdoni, B., & Sadat, R. 1999, A&A, 350, 381

Elbaz, D., et al. 1999, A&A, 351, L37

Elbaz, D., et al. 2002, A&A, 384, 848

Farrah, D., Afonso, J., Efstathiou, A., Rowan-Robinson, M., Fox, M. & Clements, D. 2003, MNRAS, 343, 585

Fioc, M., & Rocca-Volmerange, B. 1997, A&A, 326, 950

Fiore, F., et al. 2003, A&A, 409, 79

Fiore, F., et al. 2008, ApJ, 672, 94

Förster Schreiber, N.M., et al. 2003, A&A, 399, 833

Franceschini, A., et al. 2005, AJ, 129, 2074

Franceschini, A., et al. 2001, A&A, 378, 1

Gruppioni, C., et al. 2002, MNRAS, 335, 831

Gruppioni, C., Pozzi, F., Lari, C., Oliver, S., and Rodighiero, G. 2005, ApJ, 618, L9

Hacking, P.B., Houck, J.R. & Condon, J.J. 1987, ApJ, 316, 15

Hatziminaoglou, E., Pérez-Fournon, I., Polletta, M., et al. 2005, AJ, 129, 1198

Hickox, R.C., et al. 2007, ApJ, 671, 1365

Hook, I.M., Becker, R.H., McMahon, R.G., & White, R.L. 1998, MNRAS, 297, 1115

Ilbert, O., et al. 2006, A&A, 457, 841

Jarrett, T.H., Chester, T., Cutri, R., Schneider, S., Skrutskie, M., & Huchra, J.P. 2000, AJ 119, 2498

Jarrett, T. H., et al. 2006, AJ, 131, 261

Kessler M.F., et al. 1996, A&A, 315, 27

La Franca, F., et al. 2004, AJ, 127, 3075

La Franca, F., et al. 2007, A&A, in press

Lagache, G., Dole, H., & Puget, J.-L. 1999, A&A, 344, 322

Lagache, G., et al. 2004, ApJS, 154, 112

Lari, C., et al. 2001, MNRAS, 325, 1173

Le Floc′h, E., et al. 2005, ApJ, 632, 169

Lonsdale, C.J., & Hacking, P.B. 1989, ApJ, 339, 712

Lonsdale, C., et al. 2003, PASP, 115, 897

Lonsdale, C., et al. 2004, ApJS, 154, 54

Lonsdale, C., Farrah, D. & Smith, H.E., Astrophysics Update 2, 285

Maddox, S.J., Efstathiou, G., Sutherland, W.J. & Loveday, J. 1990, MNRAS, 243, 692

Maiolino, R., et al. 2006, A&A 445, 457

Marleau, F., et al. 2004, ApJS, 154, 66

Martin D.C., et al. 2005, ApJ, 619, L1

Martinez-Sansigre, A., & Rawlings, S. 2007, proc. of "The Central Engine of Active Galactic Nuclei". Eds. L.C. Ho & J.-M. Wang (San Francisco: ASP), v. 373, p. 728

Matute, I., et al. 2002, MNRAS, 332, L11

Matute, I., La Franca, F., Pozzi, F., Gruppioni, C., Lari, C., & Zamorani, G. 2006, A&A, 451, 553

Papovich, C., et al. 2004, ApJS, 154, 70

Pearson C. 2005, MNRAS, 358, 1417

Pèrez-Gonzàlez, P.G., et al. 2005, ApJ, 630, 82

Polletta, M., et al. 2006, ApJ, 642, 673

Polletta, M., et al. 2007, ApJ, 663, 81

Pozzi, F., et al. 2004, ApJ, 609, 122

Puccetti, S., et al. 2006, A&A, 457, 501

Rowan-Robinson, M., et al. 2004, MNRAS, 351, 1290

Rush, B., Malkan, M.A., & Spinoglio, L. 1993, ApJS,89, 1

Saunders, W., Rowan-Robinson, M., Lawrence, A., Efstathiou, G., Kaiser, N., Ellis, R.S., & Frenk, C.S. 1990, MNRAS, 242, 318

Silva, L., Granato, G. L., Bressan, A., & Danese, L. 1998, ApJ, 509, 103

Smith, J.D.T., et al. 2006, ApJ, 656, 770

Stern, D., et al. 2005, ApJ, 631, 163

Surace, J.A., et al. 2005, AAS, 207, 37, p.1246

Tajer, M., et al. 2007, A&A, 467, 73

Treister, E., et al., 2006, ApJ, 640, 603

Vanzella, E., et al. 2005, A&A, 434, 53

Vanzella, E., et al. 2006, A&A, 454, 423

Weedman, D., et al. 2006, ApJ, 653, 101

Werner, M.W., et al. 2004, ApJS, 154, 1

Table 1. Multiwavelength Properties of the 15 μm Sources in the ELAIS-S1 Field: Example Table

ISOCAM NAME	F_{FUV} (μJy)	F_{NUV} (μJy)	F_B (μJy)	F_V (μJy)	F_R (μJy)	F_J (μJy)	F_{Ks} (μJy)	$F_{3.6}$ (μJy)	$F_{4.5}$ (μJy)	$F_{5.8}$ (μJy)	$F_{8.0}$ (μJy)	F_{15} (mJy)	F_{24} (mJy)	F_{70} (mJy)	F_{160} (mJy)	z	L_{IR} ($L_\odot$)	Spe_cla	SED_cla
ELAISC15_J002848−430658	8.4	26.7	43.3	−	39	−	−	301	413	560	780	1.0	2.4	<15.6	<99.6	0.594	8.88×10^{12}	AGN1	AGN1
ELAISC15_J002904−425243	15.7	40.1	56.6	−	67	−	−	537	841	1186	1706	1.2	3.8	<15.6	<99.6	0.642	1.15×10^{13}	AGN1	AGN1
ELAISC15_J002904−432415	−	−	69.4	−	152	−	−	223	200	121	1182	1.4	2.1	31.3	<99.6	0.207	1.99×10^{12}	GAL	GAL
ELAISC15_J002915−430333	−	−	21.3	−	70	−	356	297	352	281	1247	1.9	4.2	57.1	175.5	0.417	2.94×10^{13}	STB	STB
ELAISC15_J002924−432233	14.1	26.7	69.4	−	195	−	470	387	298	352	2517	2.1	3.8	49.3	<99.6	0.374	2.85×10^{13}	LINER	AGN2
ELAISC15_J002925−434917	−	−	39.9	−	101	−	−	263	332	552	1249	2.9	4.5	<15.6	<99.6	3.094	1.56×10^{15}	AGN1	AGN1
ELAISC15_J002930−432726	−	−	100.3	−	171	−	525	740	972	1222	1524	1.4	2.3	<15.6	<99.6	0.914	1.95×10^{13}	AGN1	AGN1
ELAISC15_J002933−435238	38.2	219.3	91.4	−	230	−	308	840	1189	1712	2370	2.3	7.1	<15.6	<99.6	0.994	6.61×10^{13}	AGN1	AGN1
ELAISC15_J002939−430625	46.6	87.2	516.9	−	676	−	−	869	576	543	4395	3.4	3.2	51.8	196.6	0.071	6.88×10^{11}	GAL	GAL
ELAISC15_J002949−430703	1.6	1.7	24.9	−	65	−	−	467	592	700	1053	1.2	4.8	<15.6	<99.6	0.302	1.75×10^{12}	AGN2	AGN2
ELAISC15_J002959−434832	−	11.3	107.0	−	309	−	377	573	835	1524	2627	1.4	6.3	<15.6	<99.6	2.039	7.05×10^{13}	AGN1	AGN1
ELAISC15_J003001−432202	2.4	9.3	38.4	−	111	−	−	228	212	150	587	1.3	1.1	<15.6	<99.6	0.274	2.25×10^{12}	GAL	GAL
ELAISC15_J003011−432947	−	−	940.6	−	1592	−	1282	2354	1509	1492	1023	1.2	2.6	33.2	<99.6	0.084	2.50×10^{11}	GAL	GAL
ELAISC15_J003014−430332	1.6	10.6	38.8	−	96	−	−	223	385	716	1466	2.5	4.7	<15.6	<99.6	1.654	1.48×10^{14}	AGN1	AGN1
ELAISC15_J003014−434543	20.8	33.6	−	−	175	−	479	224	140	129	<32	1.1	0.8	<15.6	<99.6	0.190	8.76×10^{11}	GAL	GAL
ELAISC15_J003014−440505	4.5	8.7	74.7	−	147	−	492	301	278	208	2119	1.6	3.0	27.4	142.7	0.217	1.38×10^{12}	GAL	AGN2
ELAISC15_J003022−423657	20.6	41.3	254.3	−	708	−	2754	3088	3061	3300	16308	23.0	40.1	767.9	1181.7	0.149	1.26×10^{13}	AGN2	AGN2
ELAISC15_J003025−433056	−	−	360.9	−	875	−	−	1836	1258	614	5550	2.4	3.4	42.8	229.3	0.071	3.50×10^{11}	GAL	GAL
ELAISC15_J003039−433105	−	−	27.6	−	76	−	−	268	254	225	1259	1.4	1.5	18.8	<99.6	0.218	1.50×10^{12}	GAL	AGN2
ELAISC15_J003045−432203	16.0	28.1	377.9	−	933	−	2975	1999	1297	1388	6239	3.4	3.3	48.7	187.2	0.072	5.10×10^{11}	GAL	GAL
ELAISC15_J003054−430044	98.8	130.7	819.2	−	1349	−	−	1922	1336	748	4035	1.5	2.6	36.1	<99.6	0.071	2.14×10^{11}	AGN2	GAL
ELAISC15_J003056−435808	3.8	6.8	36.7	−	117	−	−	263	244	167	791	1.2	2.4	<15.6	<99.6	0.234	1.39×10^{12}	GAL	GAL
ELAISC15_J003058−441620	422.9	542.5	2194.8	−	3450	−	−	2994	1893	3886	9836	2.6	4.6	126.4	354.5	0.020	2.89×10^{10}	STB	GAL
ELAISC15_J003059−442133	−	−	30.8	−	119	−	614	567	691	1121	1956	2.8	5.0	<15.6	<99.6	2.101	1.81×10^{14}	AGN1	AGN2
ELAISC15_J003104−425635	149.3	196.3	1263.0	−	1636	−	−	2019	1298	1319	6785	2.4	2.8	45.4	241.0	0.071	3.49×10^{11}	GAL	GAL
ELAISC15_J003110−441715	6.6	11.4	61.5	−	167	−	387	319	257	180	1040	1.2	1.9	<15.6	<99.6	0.179	4.93×10^{11}	GAL	GAL
ELAISC15_J003114−424228	1.5	10.0	46.7	−	26	−	−	1108	1750	2546	3997	6.0	11.8	<15.6	<99.6	0.593	3.62×10^{14}	AGN1	ULIG
ELAISC15_J003123−430939	0.8	1.5	12.5	−	37	−	−	206	193	178	949	1.0	1.4	<15.6	<99.6	0.220	1.10×10^{12}	GAL	AGN2
ELAISC15_J003132−435009	1.3	−	−	−	51	−	−	156	213	274	712	1.2	2.9	19.0	<99.6	0.290	3.82×10^{12}	STB	AGN2
ELAISC15_J003133−424445	551.0	701.7	−	−	3388	−	−	3256	2151	4739	13635	4.3	7.6	151.9	491.4	0.0 26	8.29×10^{10}	GAL	GAL
ELAISC15_J003133−431939	3.2	8.9	79.6	−	226	−	608	503	360	448	3177	2.8	4.5	83.5	203.6	0.116	9.09×10^{11}	GAL	AGN2
ELAISC15_J003133−435907	48.1	43.0	48.9	−	181	−	625	834	892	901	1218	1.6	6.2	<15.6	<99.6	0.258	2.29×10^{12}	AGN2	AGN1
ELAISC15_J003135−442902	1.7	5.2	19.6	−	75	−	308	323	371	452	891	1.9	5.1	<15.6	<99.6	0.392	1.33×10^{13}	AGN2	AGN2
ELAISC15_J003136−442431	7.2	10.1	114.1	−	351	−	−	672	527	377	746	1.8	4.0	<15.6	<99.6	0.182	8.35×10^{11}	AGN2	GAL
ELAISC15_J003142−425642	−	−	−	−	26	−	−	262	304	416	671	1.2	3.0	<15.6	<99.6	0.494	4.53×10^{13}	GAL	AGN1
ELAISC15_J003142−440257	42.8	59.5	294.7	−	522	−	−	683	496	225	2163	1.1	1.6	<15.6	<99.6	0.107	4.00×10^{11}	GAL	GAL
ELAISC15_J003154−433117	−	−	86.2	105.0	110	−	−	1021	1304	1703	2084	2.4	3.8	<15.6	<99.6	0.560	1.84×10^{13}	AGN1	AGN1
ELAISC15_J003154−440932	219.8	258.6	−	−	3061	−	5151	3657	2282	4039	10704	3.7	3.8	76.0	510.1	0.033	1.18×10^{11}	GAL	GAL
ELAISC15_J003157−435401	20.0	30.6	102.5	194.0	242	−	334	321	231	173	893	3.3	<0.2	<15.6	<99.6	0.131	1.84×10^{12}	GAL	GAL
ELAISC15_J003210−442709	6.5	11.7	53.6	−	129	−	−	219	198	141	912	1.3	1.2	<15.6	<99.6	0.217	2.10×10^{12}	GAL	GAL
ELAISC15_J003212−424104	5.6	10.7	54.6	−	134	−	−	265	228	133	790	1.2	1.2	<15.6	<99.6	0.207	9.43×10^{11}	GAL	GAL
ELAISC15_J003213−434553	35.9	139.0	422.2	460.9	453	−	539	1011	1602	2692	4436	6.9	9.1	<15.6	<99.6	1.707	4.47×10^{14}	AGN1	AGN1
ELAISC15_J003220−432525	−	−	102.5	230.1	302	−	787	693	483	386	2830	2.8	3.7	53.7	139.2	0.195	3.14×10^{12}	STB	GAL
ELAISC15_J003234−431940	2.3	23.1	65.9	62.4	62	−	−	159	259	445	742	1.3	2.5	<15.6	<99.6	1.637	7.79×10^{13}	AGN1	AGN1
ELAISC15_J003237−425144	7.2	14.1	182.5	−	959	−	1076	484	285	212	<32	2.8	3.7	46.2	<99.6	0.208	2.28×10^{12}	GAL	GAL
ELAISC15_J003242−431548	−	7.4	5.9	7.9	13	47.9	88	124	94	112	84	0.6	1.0	<15.6	<99.6	0.794	3.26×10^{13}	GAL	AGN2
ELAISC15_J003243−424756	0.6	1.5	21.9	−	74	−	425	406	365	326	2698	2.4	2.4	35.8	147.4	0.192	2.14×10^{12}	GAL	GAL
ELAISC15_J003244−423313	16.9	33.3	546.2	−	1164	−	−	1700	1148	1424	8169	10.6	29.5	227.2	301.9	0.053	6.65×10^{11}	AGN2	AGN2
ELAISC15_J003248−424000	5.0	16.0	34.4	−	93	−	−	232	264	238	950	1.3	3.3	54.9	<99.6	0.369	6.76×10^{12}	STB	AGN2
ELAISC15_J003252−430716	3.9	7.0	14.9	29.6	35	−	−	54	54	<29	187	0.9	0.4	<15.6	<99.6	0.264	2.08×10^{12}	STB	GAL
ELAISC15_J003253−443150	20.3	32.0	35.4	−	50	−	−	268	285	375	462	1.0	1.4	<15.6	<99.6	0.694	1.20×10^{13}	AGN1	AGN1

Table 1—Continued

ELAISC15_J003254−424610	7.4	15.9	82.6	—	248	—	597	660	597	578	4516	7.3	17.4	163.6	244.5	0.190	6.45×10^{12}	LINER	AGN2
ELAISC15_J003257−433426	1.8	3.9	40.3	100.3	146	450.3	673	422	294	223	933	0.7	1.5	24.1	<99.6	0.180	2.91×10^{11}	GAL	GAL
ELAISC15_J003258−433145	0.6	3.3	14.6	45.0	73	—	—	195	172	109	245	0.7	0.5	<15.6	<99.6	0.289	1.08×10^{12}	GAL	GAL
ELAISC15_J003301−440748	16.2	37.8	48.4	—	62	—	—	313	440	576	917	1.7	3.0	<15.6	<99.6	0.887	3.90×10^{13}	AGN1	AGN1
ELAISC15_J003302−442952	2.6	8.1	26.6	—	54	—	—	114	115	80	229	1.3	0.5	<15.6	<99.6	0.387	1.55×10^{13}	GAL	GAL
ELAISC15_J003303−424013	3.0	6.7	57.7	—	156	—	334	318	266	216	1279	2.6	3.9	44.8	<99.6	0.184	2.19×10^{12}	GAL	AGN2
ELAISC15_J003303−425222	71.6	109.1	377.9	—	805	—	—	1054	697	659	6291	4.4	5.7	78.2	235.2	0.078	1.10×10^{12}	STB	GAL
ELAISC15_J003312−423916	7.1	12.8	72.0	—	81	—	—	176	166	99	1079	1.6	2.2	31.8	<99.6	0.220	2.71×10^{12}	GAL	GAL
ELAISC15_J003312−424936	0.9	1.7	19.8	—	51	—	—	256	241	229	1080	1.7	1.3	<15.6	<99.6	0.179	1.38×10^{12}	GAL	AGN2
ELAISC15_J003314−431522	—	2.1	17.6	53.4	82	—	—	260	231	181	1037	1.2	2.9	35.0	<99.6	0.210	1.22×10^{12}	GAL	AGN2
ELAISC15_J003316−430959	9.1	19.3	80.0	196.7	254	—	649	580	460	251	1464	1.3	2.8	40.7	<99.6	0.197	8.60×10^{11}	LINER	GAL
ELAISC15_J003317−431706	—	—	0.8	—	—	—	—	—	—	—	—	10.3	22.0	21.2	<99.6	0.689	1.50×10^{14}	GAL	ULIG
ELAISC15_J003318−431659	4.6	—	50.9	140.8	206	—	887	499	369	251	798	0.6	1.8	21.2	<99.6	0.199	4.46×10^{11}	STB	GAL
ELAISC15_J003318−442445	132.2	171.5	638.8	—	805	—	—	892	572	321	3910	1.8	2.9	45.7	200.1	0.088	4.47×10^{11}	GAL	GAL
ELAISC15_J003319−423542	13.3	25.6	—	—	1111	—	—	2145	1440	719	2880	1.3	1.8	<15.6	<99.6	0.121	5.30×10^{11}	GAL	GAL
ELAISC15_J003319−442615	22.1	—	—	—	89	—	445	638	370	445	3394	1.8	4.4	62.1	<99.6	0.089	1.58×10^{12}	STB	AGN2
ELAISC15_J003322−432633	4.6	8.5	23.1	71.5	95	210.0	319	201	205	280	915	2.1	14.1	121.8	<99.6	0.316	8.45×10^{12}	STB	STB
ELAISC15_J003327−441330	2.2	6.0	54.1	—	186	—	863	656	577	455	2606	3.0	4.0	61.3	195.4	0.232	3.42×10^{12}	GAL	AGN2
ELAISC15_J003329−431322	11.8	—	49.7	111.2	130	—	—	237	193	135	720	0.6	0.9	<15.6	<99.6	0.211	9.05×10^{11}	GAL	GAL
ELAISC15_J003330−431553	—	—	1.5	3.5	5.4	22.0	29.4	63.6	116	214	381	1.2	1.9	<15.6	<99.6	2.170	1.08×10^{15}	AGN1	ULIG
ELAISC15_J003335−431653	2.5	7.7	39.3	82.9	116	398.6	619	394	337	339	1461	0.7	1.4	<15.6	<99.6	0.150	4.07×10^{11}	GAL	AGN2
ELAISC15_J003343−441658	0.7	3.0	18.5	—	58	—	—	142	127	84	236	1.0	0.6	<15.6	<99.6	0.276	1.74×10^{12}	GAL	GAL
ELAISC15_J003346−431942	2.1	5.2	13.3	34.0	55	—	—	285	333	395	775	0.8	3.2	<15.6	<99.6	0.403	6.71×10^{12}	STB	AGN2
ELAISC15_J003347−431201	—	—	19.4	—	67	180.8	263	159	129	100	493	0.7	0.6	<15.6	<99.6	0.217	6.22×10^{11}	GAL	GAL
ELAISC15_J003348−425354	1.7	5.8	11.0	—	32	—	—	891	951	1232	1761	5.0	12.6	<15.6	<99.6	0.494	1.92×10^{14}	AGN2	ULIG
ELAISC15_J003356−432058	19.9	33.9	162.9	341.3	438	1118.6	1403	776	465	355	2025	2.0	1.7	21.4	<99.6	0.148	1.08×10^{12}	GAL	GAL
ELAISC15_J003400−441108	9.8	19.1	37.4	—	82	—	—	237	311	349	1210	1.2	6.1	124.1	159.1	0.305	9.32×10^{12}	STB	AGN2
ELAISC15_J003401−430846	—	101.7	1315.6	2553.9	3417	—	9035	4793	2968	2277	4513	1.7	2.0	40.5	202.4	0.052	2.04×10^{11}	GAL	GAL
ELAISC15_J003407−433559	1.6	2.5	9.6	26.0	38	—	147	169	186	215	354	0.6	2.0	<15.6	<99.6	0.294	1.01×10^{12}	GAL	AGN2
ELAISC15_J003407−434725	—	—	2.3	5.9	14	—	—	169	126	136	190	0.7	0.9	<15.6	<99.6	0.552	3.13×10^{13}	GAL	STB
ELAISC15_J003408−431011	7.6	36.0	48.2	56.0	61	—	—	277	359	458	707	0.8	2.1	<15.6	<99.6	1.065	1.52×10^{13}	AGN1	AGN1
ELAISC15_J003414−423152	—	—	215.4	—	762	—	1009	945	608	874	2625	4.6	10.0	90.8	<99.6	0.053	2.88×10^{11}	GAL	AGN2
ELAISC15_J003414−442206	18.7	43.3	—	—	184	—	—	214	177	74	1044	1.4	1.3	<15.6	<99.6	0.197	1.29×10^{12}	STB	GAL
ELAISC15_J003415−430235	9.1	15.8	74.0	153.7	196	—	565	391	323	250	1635	1.2	1.6	<15.6	<99.6	0.189	6.73×10^{11}	GAL	GAL
ELAISC15_J003416−430941	2.5	10.6	41.3	106.5	145	—	667	381	413	341	1662	3.1	7.8	120.6	128.7	0.313	1.24×10^{13}	STB	STB
ELAISC15_J003416−433905	16.5	27.0	268.8	534.0	711	—	—	1218	802	398	2463	0.9	1.6	19.7	<99.6	0.091	2.09×10^{11}	GAL	GAL
ELAISC15_J003417−433422	2.1	3.8	25.0	49.6	64	—	—	133	101	81	510	0.4	0.6	<15.6	<99.6	0.149	2.41×10^{11}	GAL	GAL
ELAISC15_J003421−431531	3.6	9.4	100.6	234.6	315	891.3	1223	744	519	468	2673	2.7	2.7	29.0	<99.6	0.148	1.49×10^{12}	GAL	GAL
ELAISC15_J003423−441113	13.4	22.0	114.1	—	279	—	544	395	290	258	1504	1.7	1.5	<15.6	<99.6	0.147	1.43×10^{12}	GAL	GAL
ELAISC15_J003425−423753	16.4	—	225.6	—	552	—	765	987	698	416	2747	2.0	2.0	<15.6	<99.6	0.120	1.20×10^{12}	GAL	GAL
ELAISC15_J003429−432614	61.0	—	1664.9	—	1967	7260.3	8333	5323	3595	5462	25297	21.3	21.5	310.9	967.6	0.052	1.51×10^{12}	GAL	AGN2
ELAISC15_J003432−433922	31.5	130.0	5817.7	13390.8	17543	—	38012	<3	15892	12690	11998	5.4	3.3	110.8	494.9	0.020	8.32×10^{10}	GAL	GAL
ELAISC15_J003439−432654	19.0	27.8	174.4	300.8	401	—	751	549	342	501	2148	1.7	6.0	38.3	<99.6	0.053	1.24×10^{11}	GAL	GAL
ELAISC15_J003441−433041	6.9	14.0	30.5	102.5	138	360.7	577	275	272	251	770	1.3	3.1	39.4	181.4	0.160	8.01×10^{11}	GAL	AGN2
ELAISC15_J003441−441327	17.7	30.6	238.4	—	303	—	758	881	1037	1408	3093	6.6	18.8	123.0	196.6	0.125	2.50×10^{12}	AGN2	AGN2
ELAISC15_J003447−425207	1.9	4.7	119.5	—	215	—	534	436	361	371	1366	1.7	6.4	47.9	<99.6	0.122	6.28×10^{11}	LINER	AGN2
ELAISC15_J003447−432447	—	0.5	0.7	1.2	2	17	41	97	130	189	370	0.6	0.9	<15.6	<99.6	1.076	8.29×10^{13}	AGN2	ULIG
ELAISC15_J003458−425733	60.7	131.4	720.1	—	2387	—	2703	3822	2593	4035	19030	14.4	35.4	373.5	707.9	0.055	9.79×10^{11}	GAL	AGN2
ELAISC15_J003459−425637	4.1	13.1	—	—	37	—	—	183	262	215	1117	1.2	4.6	58.7	<99.6	0.330	4.91×10^{12}	STB	STB
ELAISC15_J003501−423914	6.8	11.4	308.6	—	942	—	2208	2305	1556	1798	8228	6.6	15.7	258.7	493.7	0.052	3.95×10^{11}	GAL	AGN2
ELAISC15_J003502−432411	15.2	28.4	69.3	157.1	182	—	—	236	217	160	924	1.4	1.5	<15.6	<99.6	0.227	2.65×10^{12}	GAL	GAL
ELAISC15_J003503−431138	3.0	11.7	47.8	131.2	175	—	470	424	342	267	1665	1.0	2.2	<15.6	<99.6	0.176	4.02×10^{11}	GAL	GAL
ELAISC15_J003503−432117	37.2	57.4	209.0	453.7	537	—	—	869	624	304	2579	1.5	2.1	34.1	<99.6	0.146	1.31×10^{12}	GAL	GAL
ELAISC15_J003505−430752	—	—	6.0	20.5	32	—	398	178	190	159	634	0.9	1.7	27.8	<99.6	0.322	1.56×10^{12}	GAL	STB

Table 1—Continued

ELAISC15_J003507−431236	3.9	8.1	36.2	87.2	107	−	−	173	139	105	540	0.5	0.5	<15.6	<99.6	0.177	2.02×10^{11}	GAL	GAL
ELAISC15_J003511−422928	3.6	15.2	63.8	−	191	−	631	431	364	270	1646	1.6	2.2	23.1	<99.6	0.204	1.21×10^{12}	GAL	AGN2
ELAISC15_J003511−435906	−	154.7	−	−	11217	−	−	14400	8415	8109	9664	12.7	7.5	183.3	834.2	0.024	2.22×10^{11}	GAL	GAL
ELAISC15_J003512−431540	−	−	7.4	29.5	47	199.6	453	293	287	192	847	0.9	1.6	50.6	<99.6	0.275	1.79×10^{13}	GAL	STB
ELAISC15_J003513−433540	3.1	7.1	111.5	388.3	562	2112.1	3112	1510	1080	513	1410	1.7	1.2	<15.6	158.0	0.147	1.43×10^{12}	GAL	GAL
ELAISC15_J003515−433356	262.0	315.5	456.6	635.6	634	−	2466	2950	3661	4824	8905	15.2	27.7	94.4	<99.6	0.143	2.59×10^{12}	AGN1	AGN1
ELAISC15_J003517−431121	21.5	43.7	119.7	290.8	364	−	1459	645	410	334	1217	1.1	2.3	18.1	<99.6	0.175	6.79×10^{11}	GAL	GAL
ELAISC15_J003517−434252	36.7	55.0	131.5	236.5	260	−	−	364	159	155	935	1.1	1.1	<15.6	<99.6	0.148	7.65×10^{11}	GAL	GAL
ELAISC15_J003519−431325	4.2	6.4	28.7	110.3	166	−	−	601	504	368	1385	2.3	5.0	49.1	<99.6	0.279	3.70×10^{12}	GAL	AGN2
ELAISC15_J003519−433711	5.8	14.7	37.9	109.9	146	407.1	745	418	371	295	1191	1.6	3.6	64.0	211.8	0.286	2.74×10^{12}	GAL	AGN2
ELAISC15_J003519−440446	−	−	−	−	9797	−	2012	9797	5938	2101	1580	8.1	2.3	75.9	590.9	0.025	1.43×10^{11}	UNCL	GAL
ELAISC15_J003520−433645	1.5	3.9	41.6	111.4	157	537.9	879	753	831	1029	2790	1.8	4.6	51.3	<99.6	0.149	1.00×10^{12}	GAL	AGN2
ELAISC15_J003521−432447	7.0	11.0	66.9	131.5	172	392.5	471	306	214	275	2122	2.0	4.1	42.3	43.9	0.089	3.80×10^{11}	STB	AGN2
ELAISC15_J003523−432514	0.3	1.5	10.2	36.3	50	−	340	152	166	114	584	0.8	1.8	29.1	87.9	0.283	1.35×10^{12}	GAL	AGN2
ELAISC15_J003526−435640	6.4	16.0	7.1	58.0	106	−	−	244	256	193	741	1.5	1.9	24.5	<99.6	0.324	2.81×10^{12}	GAL	AGN2
ELAISC15_J003529−424311	1.4	2.3	45.4	−	119	−	466	379	342	237	1175	1.5	1.6	<15.6	<99.6	0.221	1.59×10^{12}	GAL	AGN2
ELAISC15_J003529−430746	0.6	4.6	16.5	52.0	71	−	−	<3	145	94	735	0.8	0.7	<15.6	<99.6	0.201	5.89×10^{11}	GAL	GAL
ELAISC15_J003530−430115	33.6	54.2	191.7	364.0	410	−	719	576	341	295	2561	2.1	2.3	26.3	<99.6	0.146	1.79×10^{12}	GAL	GAL
ELAISC15_J003530−435604	6.1	14.5	107.4	280.5	374	−	1117	1024	785	612	4533	4.3	4.3	58.5	228.2	0.147	2.36×10^{12}	GAL	AGN2
ELAISC15_J003531−434448	7.6	19.4	37.4	104.9	142	−	377	241	219	113	514	0.6	0.9	<15.6	<99.6	0.286	1.97×10^{12}	GAL	GAL
ELAISC15_J003541−433302	0.4	10.4	17.6	27.5	41	−	−	212	141	170	157	1.6	1.8	31.1	<99.6	0.716	9.71×10^{13}	STB	AGN2
ELAISC15_J003545−431833	−	1.4	5.8	5.5	7	−	−	108	84	58	<32	0.6	0.6	<15.6	<99.6	1.300	1.30×10^{14}	UNCL	AGN2
ELAISC15_J003545−433216	5.0	11.5	14.7	34.8	45	109.2	189	165	204	207	727	1.6	8.3	67.6	<99.6	0.399	1.93×10^{13}	STB	STB
ELAISC15_J003546−430341	14.5	24.4	121.4	280.2	352	−	780	689	423	344	2212	1.7	2.7	30.3	<99.6	0.147	9.23×10^{11}	GAL	GAL
ELAISC15_J003546−442405	20.8	45.7	153.2	−	311	−	−	410	217	143	1007	1.3	1.6	<15.6	<99.6	0.146	8.55×10^{11}	AGN2	GAL
ELAISC15_J003548−430640	1.6	6.8	13.4	29.4	43	89.3	156	102	113	103	337	0.7	0.9	<15.6	<99.6	0.426	1.74×10^{13}	STB	AGN2
ELAISC15_J003550−430505	−	−	4.1	11.5	23	−	−	495	749	1340	2049	0.9	4.5	<15.6	<99.6	0.425	2.10×10^{13}	AGN2	ULIG
ELAISC15_J003603−433152	1.9	3.7	2.6	5.6	9	59.7	159	591	896	1391	2346	4.0	8.4	<15.6	<99.6	0.860	5.49×10^{14}	AGN1	ULIG
ELAISC15_J003603−435602	9.5	19.3	106.6	266.4	340	956.1	1274	793	442	360	2413	2.7	2.3	33.5	<99.6	0.148	1.45×10^{12}	GAL	GAL
ELAISC15_J003611−423238	3.2	11.2	−	−	176	−	544	420	328	259	2054	2.3	2.8	59.3	163.8	0.207	1.82×10^{12}	GAL	AGN2
ELAISC15_J003613−440708	3.6	7.1	81.9	−	250	−	625	572	358	354	2287	2.2	2.0	27.4	<99.6	0.107	7.10×10^{11}	GAL	AGN2
ELAISC15_J003615−431327	−	−	10.0	37.4	58	−	−	<3	181	168	298	0.5	1.1	<15.6	<99.6	0.330	4.69×10^{12}	GAL	AGN2
ELAISC15_J003618−424343	110.9	142.2	137.2	−	385	−	685	631	482	597	4518	5.6	17.0	172.8	273.8	0.115	2.26×10^{12}	STB	STB
ELAISC15_J003619−432608	10.5	18.0	129.0	277.9	343	−	−	482	233	231	1318	1.9	6.2	22.3	<99.6	0.106	5.85×10^{11}	GAL	GAL
ELAISC15_J003622−432826	−	−	0.6	2.9	7	−	−	170	172	290	687	0.6	2.7	<15.6	<99.6	0.863	8.85×10^{13}	AGN2	ULIG
ELAISC15_J003623−432702	−	0.3	2.3	6.0	13	−	−	124	88	91	95	0.6	0.6	<15.6	<99.6	0.590	1.32×10^{13}	GAL	AGN2
ELAISC15_J003626−441140	32.4	60.8	374.4	−	790	−	2772	2770	2924	4617	9063	12.4	28.4	164.7	182.5	0.088	2.28×10^{12}	AGN2	AGN2
ELAISC15_J003635−430132	8.2	18.5	77.9	202.8	265	−	705	598	481	350	1961	3.4	2.9	39.9	149.8	0.208	2.73×10^{12}	GAL	GAL
ELAISC15_J003640−433925	0.8	2.4	2.3	4.8	8	−	−	347	524	745	1086	0.8	4.2	24.7	<99.6	1.181	7.24×10^{13}	AGN1	ULIG
ELAISC15_J003645−440720	150.4	229.6	−	−	2546	−	−	3181	1960	1925	7928	4.3	5.3	75.4	308.9	0.059	3.96×10^{11}	GAL	GAL
ELAISC15_J003649−431018	12.6	20.3	49.1	104.4	127	−	−	267	237	240	1639	1.6	6.6	60.4	<99.6	0.194	6.00×10^{12}	STB	AGN2
ELAISC15_J003656−434312	3.4	9.0	10.9	29.8	42	−	−	90	80	48	128	0.9	0.5	<15.6	<99.6	0.376	7.05×10^{12}	GAL	GAL
ELAISC15_J003703−423923	1.7	4.6	22.3	−	104	−	544	521	478	413	817	1.0	2.4	33.8	<99.6	0.326	1.93×10^{12}	GAL	AGN2
ELAISC15_J003707−425114	9.6	20.0	168.0	−	336	−	649	696	588	291	990	1.2	1.9	32.1	<99.6	0.220	1.18×10^{12}	GAL	GAL
ELAISC15_J003715−423515	3.5	10.8	70.0	−	132	−	−	203	335	678	1387	3.1	6.1	<15.6	<99.6	2.190	1.42×10^{14}	AGN1	AGN1
ELAISC15_J003716−434153	11.9	29.0	69.3	171.0	207	−	−	394	258	148	950	1.0	2.3	<15.6	<99.6	0.226	2.00×10^{12}	GAL	GAL
ELAISC15_J003718−421924	10.6	31.3	35.4	−	198	−	−	299	305	295	725	2.8	3.7	41.8	156.8	0.342	2.63×10^{13}	AGN2	AGN2
ELAISC15_J003721−434239	14.9	21.4	91.1	240.9	322	−	692	892	1080	1276	3678	9.4	27.7	79.5	163.8	0.225	1.04×10^{13}	AGN2	AGN2
ELAISC15_J003724−422446	−	−	−	−	25	−	−	86	55	<29	<32	1.1	<0.2	<15.6	<99.6	0.587	5.41×10^{13}	AGN2	STB
ELAISC15_J003728−423314	18.9	52.5	48.9	−	84	−	−	417	527	698	919	2.1	3.1	<15.6	<99.6	0.994	5.97×10^{13}	AGN1	AGN1
ELAISC15_J003729−424607	2.5	7.1	36.4	−	101	−	370	327	358	284	1334	1.9	4.1	35.8	<99.6	0.291	3.37×10^{12}	STB	AGN2
ELAISC15_J003731−440812	104.6	167.0	1792.2	−	3118	−	−	5298	3455	3925	13134	10.4	9.9	97.7	490.2	0.052	7.27×10^{11}	AGN2	AGN2
ELAISC15_J003734−433342	−	7.6	34.8	127.6	194	−	501	520	532	529	1871	2.1	7.2	84.1	<99.6	0.226	2.40×10^{12}	AGN2	AGN2
ELAISC15_J003739−425038	102.7	139.3	374.4	−	790	−	−	800	544	518	4252	3.2	7.2	66.7	166.1	0.059	3.43×10^{11}	STB	GAL

Table 1—Continued

Name																			
ELAISC15_J003741−440226	2.0	4.9	16.9	−	31	−	−	117	154	219	929	1.2	7.5	178.6	<99.6	0.348	3.51×10^{12}	LINER	AGN2
ELAISC15_J003753−433937	2.5	5.6	22.8	53.0	67	−	−	129	126	104	604	0.8	1.0	<15.6	<99.6	0.223	8.59×10^{11}	GAL	GAL
ELAISC15_J003754−441106	−	−	−	−	61	−	−	235	275	416	1612	7.0	9.5	51.5	113.8	0.212	3.22×10^{13}	LINER	STB
ELAISC15_J003802−423329	2.2	5.4	61.0	−	257	−	745	545	358	243	872	1.4	1.0	<15.6	<99.6	0.233	1.74×10^{12}	GAL	GAL
ELAISC15_J003805−424106	32.7	52.0	65.6	−	159	−	−	620	754	1090	1573	3.8	4.7	<15.6	<99.6	0.415	1.43×10^{13}	AGN1	AGN1
ELAISC15_J003805−433758	1.5	2.8	−	−	63	−	598	1414	1948	2687	3804	3.2	11.8	44.0	<99.6	0.222	2.37×10^{12}	AGN2	AGN2
ELAISC15_J003806−425512	50.2	83.6	577.3	−	1230	−	−	1571	1036	1314	6821	4.9	11.7	108.3	166.1	0.045	2.55×10^{11}	STB	GAL
ELAISC15_J003813−433315	13.3	57.0	164.8	178.8	211	−	−	469	706	981	1442	1.1	2.8	<15.6	<99.6	1.400	4.46×10^{13}	AGN1	AGN1
ELAISC15_J003817−422352	58.1	92.8	347.8	−	542	−	−	<3	<5	<29	<32	1.7	<0.2	<15.6	<99.6	0.094	4.70×10^{11}	GAL	GAL
ELAISC15_J003818−421545	15.5	26.9	55.6	−	239	−	−	<3	<5	<29	<32	2.1	<0.2	<15.6	<99.6	0.115	8.98×10^{11}	STB	AGN2
ELAISC15_J003828−433848	−	390.7	1964.0	3076.1	3831	−	−	6584	4443	9856	43051	42.5	27.2	545.2	1485.9	0.048	3.88×10^{12}	UNCL	AGN2
ELAISC15_J003829−434454	−	75.2	291.8	290.5	299	−	387	768	1247	2138	3451	5.9	11.7	32.8	135.7	1.567	3.11×10^{14}	AGN1	AGN1
ELAISC15_J003834−442124	−	2.6	−	−	199	−	−	185	136	182	131	1.5	1.5	26.7	176.7	0.587	3.34×10^{13}	GAL	AGN2
ELAISC15_J003841−431906	8.9	14.6	21.4	33.9	46	−	−	207	237	<29	532	0.7	2.3	<15.6	<99.6	0.315	6.30×10^{12}	AGN1	AGN2
ELAISC15_J003848−431146	−	1.2	21.3	58.7	87	−	−	153	151	256	781	2.1	7.8	53.2	<99.6	0.126	1.06×10^{12}	UNCL	STB
ELAISC15_J003848−432305	0.3	8.0	9.6	18.9	37	−	−	126	112	85	116	1.0	0.6	<15.6	<99.6	0.537	3.30×10^{13}	GAL	GAL
ELAISC15_J003857−424417	92.1	141.7	249.6	−	695	−	608	<3	<5	<29	<32	7.2	9.0	<15.6	349.8	0.097	7.64×10^{12}	STB	AGN1
ELAISC15_J003858−424402	22.5	36.0	94.9	−	224	−	−	<3	<5	<29	<32	2.1	3.0	<15.6	<99.6	0.097	2.19×10^{12}	STB	AGN2
ELAISC15_J003859−433936	35.0	51.0	192.1	336.6	393	−	720	490	240	193	1308	2.0	1.2	<15.6	<99.6	0.119	9.15×10^{11}	GAL	GAL
ELAISC15_J003905−441603	0.4	1.0	30.0	−	62	−	−	235	196	141	1077	0.9	1.1	<15.6	<99.6	0.178	3.64×10^{11}	GAL	AGN2
ELAISC15_J003909−423312	4.1	8.0	51.6	−	125	−	340	<3	<5	<29	<32	1.4	<0.2	<15.6	<99.6	0.148	7.59×10^{11}	GAL	GAL
ELAISC15_J003913−431205	96.1	138.8	545.9	872.5	1071	−	−	1184	771	607	5440	4.1	4.2	56.5	216.5	0.057	4.02×10^{11}	STB	GAL
ELAISC15_J003915−430426	313.7	1487.6	−	12451.1	15707	−	−	23710	15377	35779	66310	58.0	75.5	1026.5	3685.5	0.013	3.42×10^{11}	UNCL	GAL
ELAISC15_J003920−424107	8.7	15.6	76.8	−	193	−	325	<3	<5	−	<32	11.1	<0.2	<15.6	<99.6	0.127	4.64×10^{12}	AGN2	STB
ELAISC15_J003921−441134	4.6	14.0	64.4	−	181	−	711	526	462	455	1448	1.9	3.2	<15.6	<99.6	0.189	1.69×10^{12}	GAL	AGN2
ELAISC15_J003922−433825	2.7	16.5	32.7	81.5	108	−	−	324	260	248	1661	1.7	2.2	34.8	148.6	0.149	9.30×10^{11}	GAL	AGN2
ELAISC15_J003932−441130	26.6	59.6	128.6	−	503	−	1202	938	699	595	3862	5.0	12.3	132.2	<99.6	0.185	4.42×10^{12}	STB	AGN2
ELAISC15_J003938−433755	5.9	12.3	169.4	499.8	603	−	1000	1057	899	860	1507	3.4	4.7	<15.6	<99.6	0.125	1.28×10^{12}	AGN2	AGN2
ELAISC15_J003940−431125	48.2	71.5	95.1	109.5	134	−	−	265	429	530	1499	3.9	13.2	68.9	<99.6	0.231	2.19×10^{13}	STB	AGN1
ELAISC15_J003942−435403	7.0	13.0	76.5	189.3	239	−	586	444	304	264	1702	1.3	2.2	24.9	<99.6	0.149	7.16×10^{11}	GAL	GAL
ELAISC15_J003945−440823	0.8	2.0	−	−	20	−	−	401	822	1695	3468	5.6	12.4	54.6	<99.6	0.590	6.66×10^{14}	AGN2	ULIG
ELAISC15_J003948−431419	7.4	14.3	−	−	202	−	614	457	328	208	1005	1.4	1.7	<15.6	<99.6	0.215	1.24×10^{12}	GAL	GAL
ELAISC15_J003951−431342	27.6	46.3	211.5	−	400	−	661	650	368	335	2343	2.0	3.1	36.7	<99.6	0.121	1.18×10^{12}	GAL	GAL
ELAISC15_J003954−440510	9.5	13.7	28.4	−	77	−	461	654	889	1191	1714	3.2	5.0	<15.6	<99.6	0.331	3.70×10^{13}	STB	ULIG
ELAISC15_J003957−432013	19.0	49.1	194.7	−	375	−	−	693	460	325	2904	2.7	2.8	33.5	<99.6	0.128	1.84×10^{12}	GAL	GAL
ELAISC15_J004009−434424	1.9	1.6	20.5	−	64	−	−	211	286	465	918	2.4	4.3	<15.6	<99.6	0.188	2.08×10^{12}	AGN2	AGN2
ELAISC15_J004011−432043	−	−	30.0	−	75	−	−	154	164	86	659	1.6	1.3	<15.6	<99.6	0.268	4.07×10^{12}	LINER	GAL
ELAISC15_J004014−432010	−	−	149.0	−	393	−	−	949	894	445	2638	2.5	4.1	45.6	214.1	0.265	6.08×10^{12}	GAL	GAL
ELAISC15_J004023−440027	−	−	17.2	−	93	−	−	314	295	246	697	1.3	1.8	16.2	<99.6	0.345	1.20×10^{13}	GAL	AGN2
ELAISC15_J004028−434017	24.9	46.3	36.4	−	61	−	−	426	588	885	1251	1.7	3.1	<15.6	<99.6	0.869	3.69×10^{13}	AGN1	AGN1
ELAISC15_J004032−440317	1.9	4.9	15.0	−	40	−	−	167	204	173	757	1.2	2.0	21.2	<99.6	0.345	3.10×10^{12}	STB	AGN2
ELAISC15_J004043−440852	2.6	5.9	22.3	−	67	−	−	314	325	339	654	1.6	2.6	<15.6	<99.6	0.363	7.72×10^{12}	AGN2	AGN2
ELAISC15_J004055−441249	2.1	5.6	34.7	−	29	−	−	356	622	1020	1758	2.6	5.4	<15.6	<99.6	1.380	6.52×10^{14}	AGN1	ULIG
ELAISC15_J004110−440250	21.5	33.0	138.4	−	232	−	−	256	182	183	1303	1.6	1.5	<15.6	<99.6	0.125	8.13×10^{11}	GAL	GAL

Table 2.   Spectroscopic Classification versus SED classification

SED ⇓ \ SPEC ⇒	Tot	AGN1	AGN2+LINER	Starburst	Galaxy	Unclass
Tot	203	27	25+7	32	107	5
AGN1	24	20 (74.1%)	1+0 (3.1%)	2 (6.2%)	1 (0.9%)	0
AGN2	72	3 (11.1%)	14+4 (56.3%)	14 (43.8%)	35 (32.8%)	2 (40.0%)
AGN+Starburst	11	4 (14.8%)	5+0 (15.6%)	1 (3.1%)	1 (0.9%)	0
Starburst	13	0	2+1 (9.4%)	6 (18.8%)	3 (2.8%)	1 (20.0%)
Galaxy	83	0	3+2 (15.6%)	9 (28.1%)	67 (62.6%)	2 (40.0%)
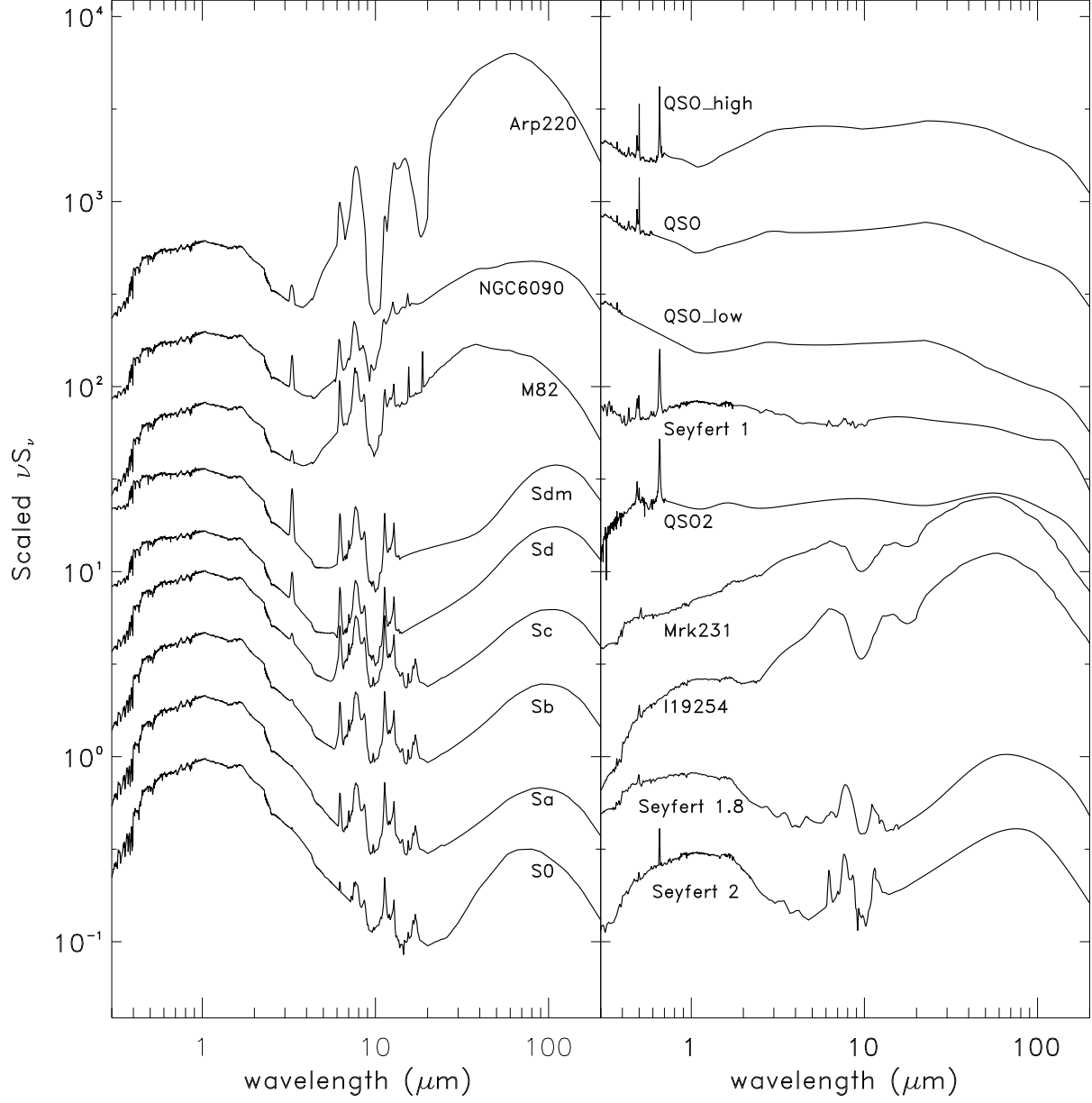
Fig. 1.— Library of template SEDs from Polletta et al. (2007). The SEDs are plotted in arbitrarily scaled luminosity νS_ν versus wavelength.
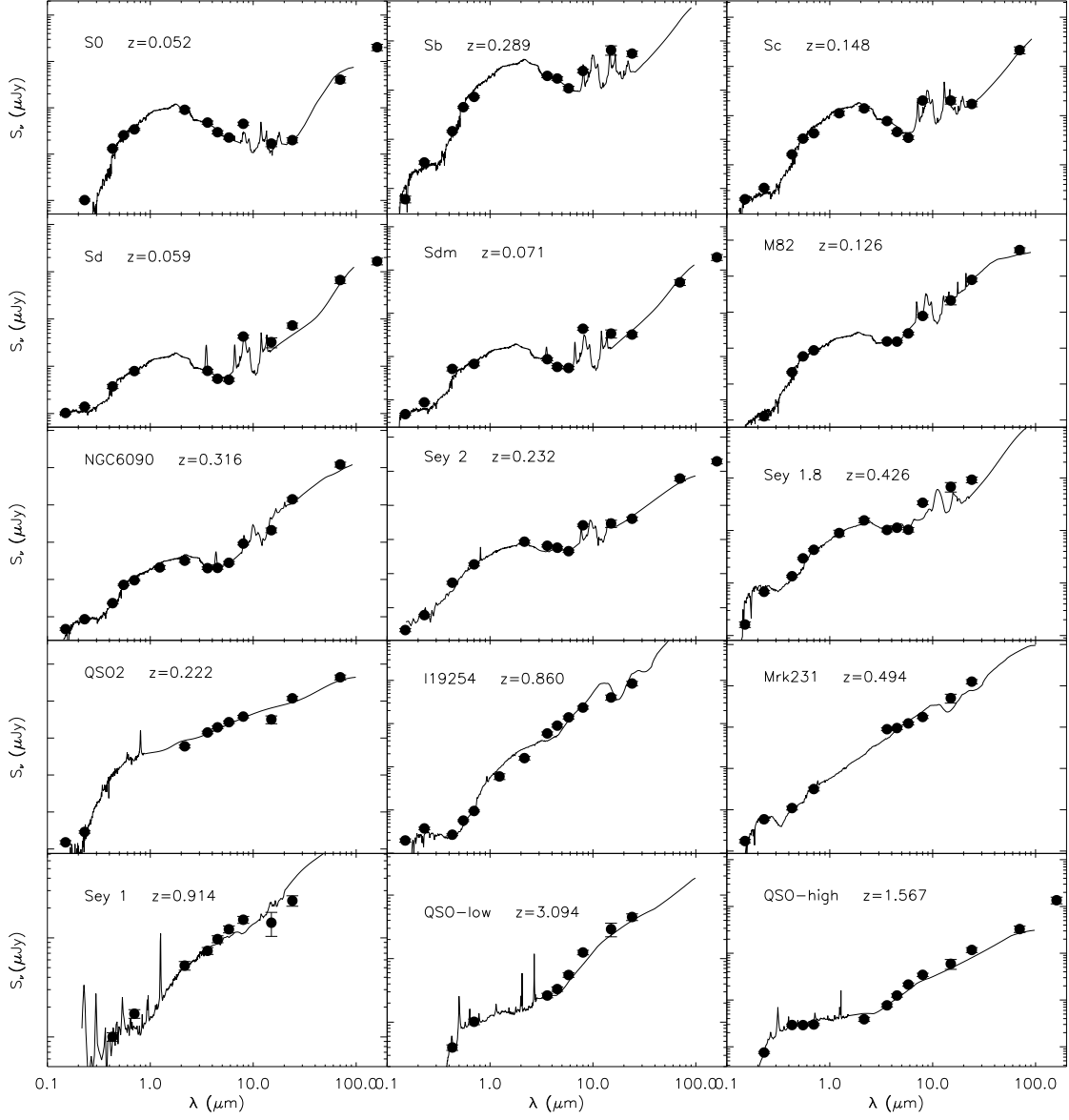
Fig. 2.— Example of SED fits for our sample: the data (filled circles with error-bars), plotted as flux (S_ν in μJy) versus observed wavelength, are over-imposed to the corresponding best-fitting template SEDs (solid line), opportunely redshifted at the source's z. The plotted uncertainties are those reported in the various catalogues and not those used for the fits.
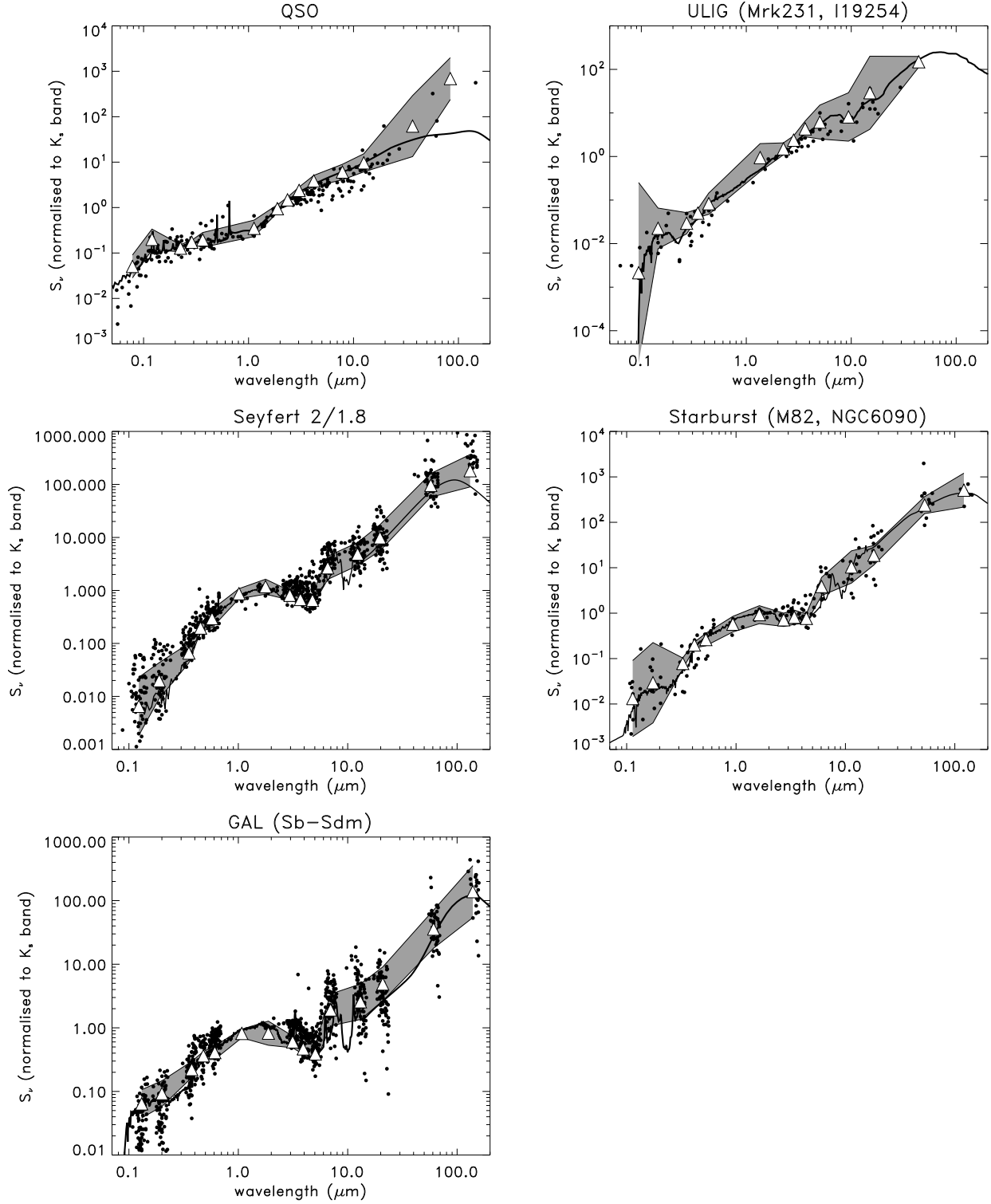
Fig. 3.— Rest-frame SEDs (dots) of 15-μm sources belonging to the different broad SED classes (AGN1, ULIG, AGN2, Starburst and Spiral galaxy) compared to the most frequent best-fit template SED of that class, all normalised to the Ks-band flux density. The white triangles represent the average values that the templates should have in the different rest-frame bands to better reproduce our sources, while the grey-shaded areas show their relative uncertainty region corresponding to $\pm 1\sigma$.
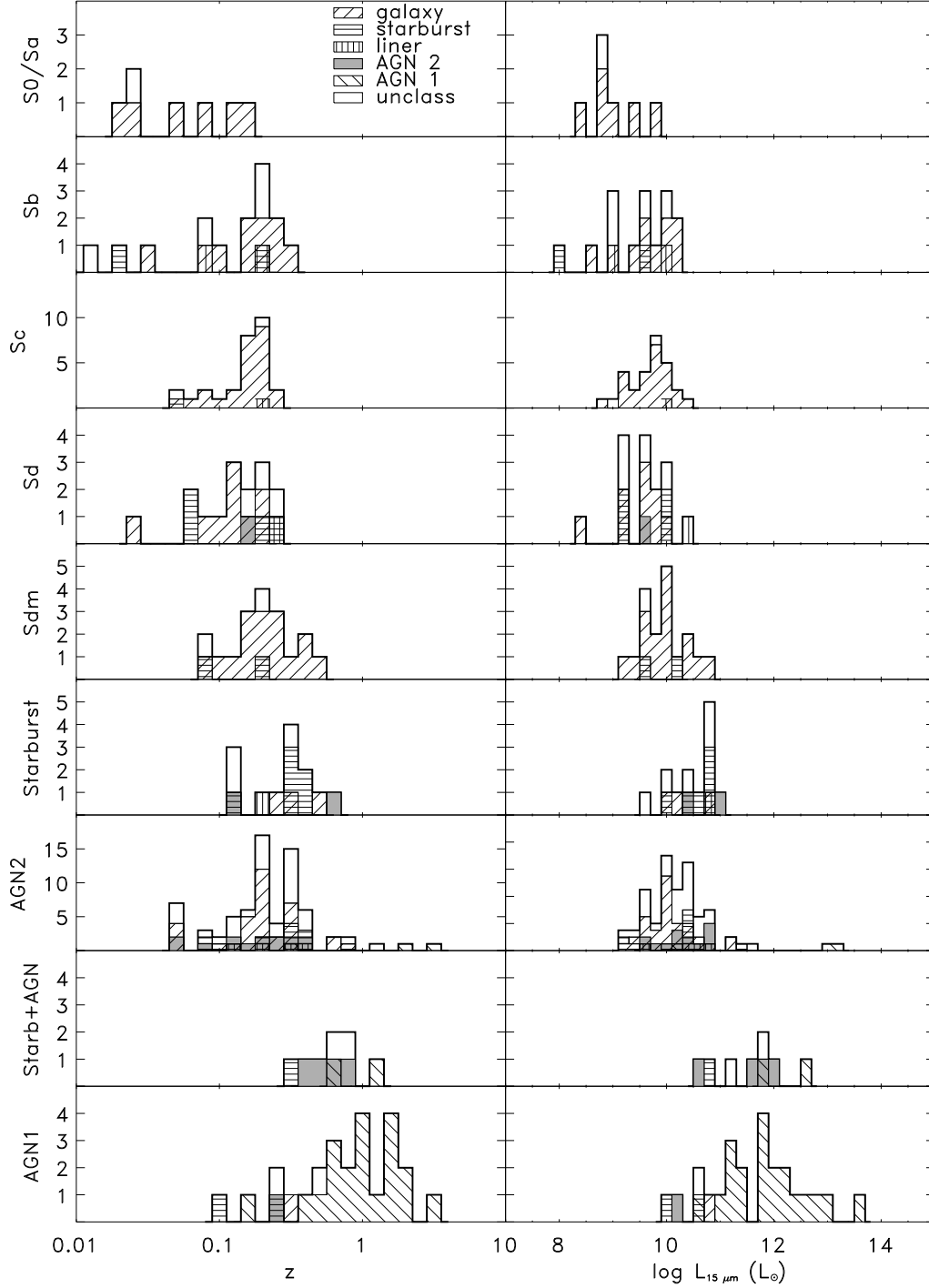
Fig. 4.— Logarithmic distributions of z ($left$) and $L_{15\mu m}$ luminosity ($right$) for the different SED classes reproducing our data. The luminosities have been derived by considering for each source its best-fitting template SED. Within each distribution the different spectroscopic classes are highlighted, as explained in the legend.
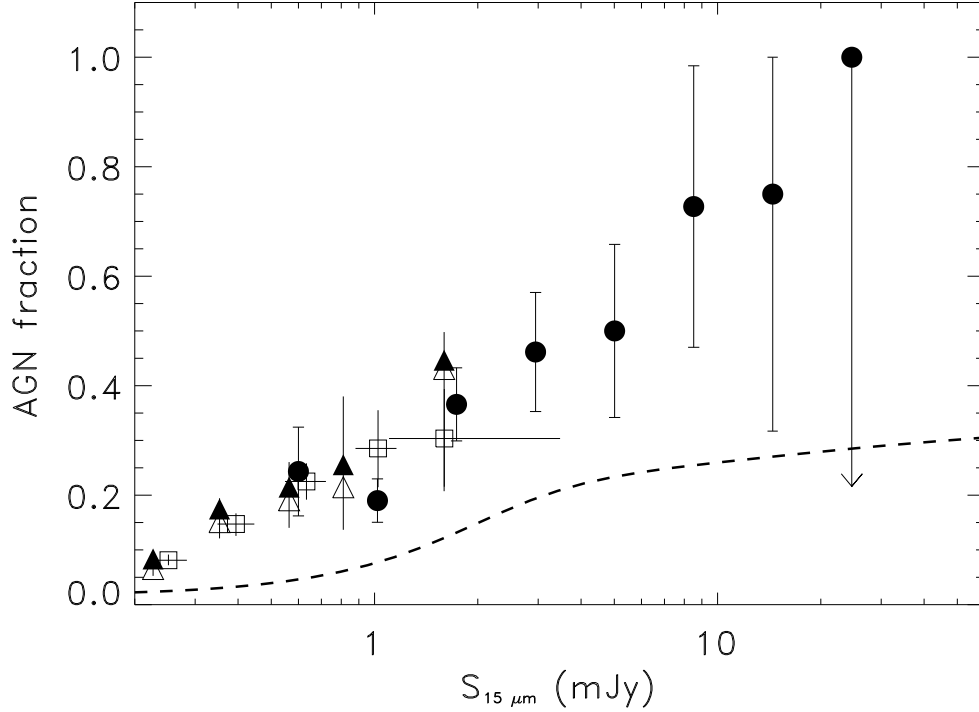
Fig. 5.— Fraction of AGN over total extragalactic sources as a function of the 15-μm flux density, as derived from the spectroscopic classification (dashed line; Matute et al. 2006) and from the SED-fitting performed in this work (filled circles with error-bars). For comparison, the results of Brand et al. (2006) and Treister et al. (2006) have been plotted as open squares and triangles (open: non corrected for AGN not detected in X-rays; filled: corrected for AGN not detected in X-rays), respectively.
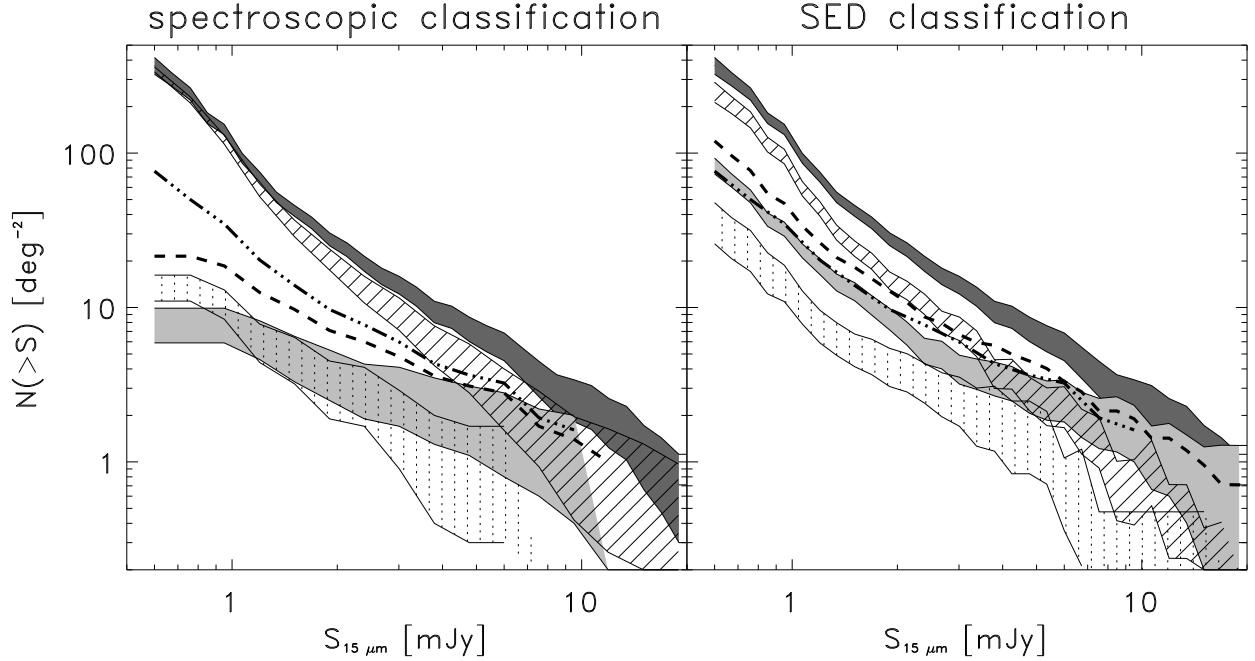
Fig. 6.— Observed extragalactic source counts at 15 μm in ELAIS-S1: total counts with uncertainties (dark-grey shaded area); type 2 AGN contribution (light-grey shaded area); type 1 AGN contribution (dotted area); galaxy contribution (hatched area). The total (type 1 + type 2) AGN contribution is shown by the dashed line, while the dot-dot-dashed line represents the total AGN counts at 15 μm updated by La Franca et al. (2007) on the basis of hard X-ray observations. In the *left* panel the AGN/galaxy contributions are derived from the spectroscopic classification (La Franca et al. 2004), while in the *right* panel they come from the SED-fitting work described in this paper. All the optically unidentified sources have been conservatively considered as galaxies in both plots (see Section 5).